January 2008

A Synergistic Approach to Modeling Crack Propagation in Nanoreinforced Polymer Composites

Andy Mccarron
University of Massachusetts Amherst, amccarro@student.umass.edu

A SYNERGISTIC APPROACH TO MODELING CRACK PROPAGATION IN NANOREINFORCED POLYMER COMPOSITES

A Thesis Presented

by

ANDREW P. MCCARRON

Submitted to the Graduate School of the
University of Massachusetts Amherst in partial fulfillment
of the requirements for the degree of

MASTER OF SCIENCE IN MECHANICAL ENGINEERING

May 2008

Mechanical and Industrial Engineering

A SYNERGISTIC APPROACH TO MODELING CRACK PROPAGATION IN NANOREINFORCED POLYMER COMPOSITES

A Thesis Presented

by

ANDREW P. MCCARRON

Approved as to style and content by:

_____
Robert W. Hyers, Chair

_____
Moon K. Kim, Member

_____
Karl Jakus, Member

_____
Mario Rotea, Department Head
Mechanical & Industrial Engineering

ACKNOWLEDGEMENTS

I would like to thank Professor Robert Hyers for his constant support, patience, and guidance throughout my academic career at the University of Massachusetts Amherst. Professor Hyers is a remarkable personal and it has been a privilege to both work and study under him. I would also like to thank the members of my thesis committee Professor Moon Kim and Professor Karl Jakus for their assistance and insight along the way. Lastly, I would like to thank my family and friends. I can't thank you enough for all you've done for me.

ABSTRACT

A SYNERGISTIC APPROACH TO MODELING CRACK PROPAGATION IN NANOREINFORCED POLYMER COMPOSITES

MAY 2008

ANDREW P. MCCARRON, B.S., UNIVERSITY OF MASSACHUSETTS AMHERST

M.S.M.E., UNIVERSITY OF MASSACHUSETTS AMHERST

Directed by: Professor Robert W. Hyers

Empirical studies indicate that a polymer reinforced with micro- and nano-scale particles could enhance both the stiffness and toughness of the composite. In addition to these augmented attributes, the composite would be light weight with a high resistance to corrosion making such a material extremely versatile and desirable for a host of applications.

Validated computational models that can accurately simulate the effects of micro- and nanoparticle reinforcement on the fracture characteristics of polymer composites are necessary to give insight into how and why this method of reinforcement is effective. Furthermore, a model that can account for non-continuum effects will hasten the development of both new hierarchical composite materials and new theories to explain their behavior[1]. This paper proposes a hierarchal method for modeling fracture in multiscale polymer composites by utilizing an Elastic Network Model (ENM) in conjunction with a Finite Element Analysis (FEA). The novelty of this approach lies in its ability to model a large part with FEA while still accounting for the interactions between the reinforcement particles and the polymer matrix at a scale below the limit of

continuum mechanics with the ENM. The intent of the research proposed in this paper is to determine the feasibility of the hierarchical modeling system.

TABLE OF CONTENTS

LIST OF TABLES

Table Page

LIST OF FIGURES

Figure Page

CHAPTER 1

BACKGROUND OF FRACTURE MECHANICS

1.1 Relevance

Crack initiation and growth are the primary causes for mechanical failure in stressed members. Cracks weaken a part by reducing the overall load bearing area and causing an increased localized stress in the material around the tip of the crack. Unexpected failure of a part during its lifetime can be costly for a number of reasons both financial and in terms of human life.

The goal of fracture mechanics is to determine what conditions will create and drive a crack. By understanding the phenomena of fracture engineers can competently design against this particular mode of failure.

1.2 Observations of Fracture

Consider an infinite thin plate under tension with a crack extending into one side, Figure 1.1. This singular crack has an enormous effect on the stress gradients throughout the part. To start with, the section of material along line A in Figure 1.1 is under a larger stress than the remainder of the block due to the decreased surface area over which the load is distributed. More importantly, the tip of the crack acts as a stress intensifier and the resulting stresses in the vicinity of the crack tip are exceedingly high. The high stress around the crack tip cause the material to plastically deformed.

The field of fracture mechanics divides materials into two broad categories, brittle and ductile, based on the materials' fracture characteristics. Brittle materials fracture with only a small amount of plastic deformation occurring. The amount of plastic deformation

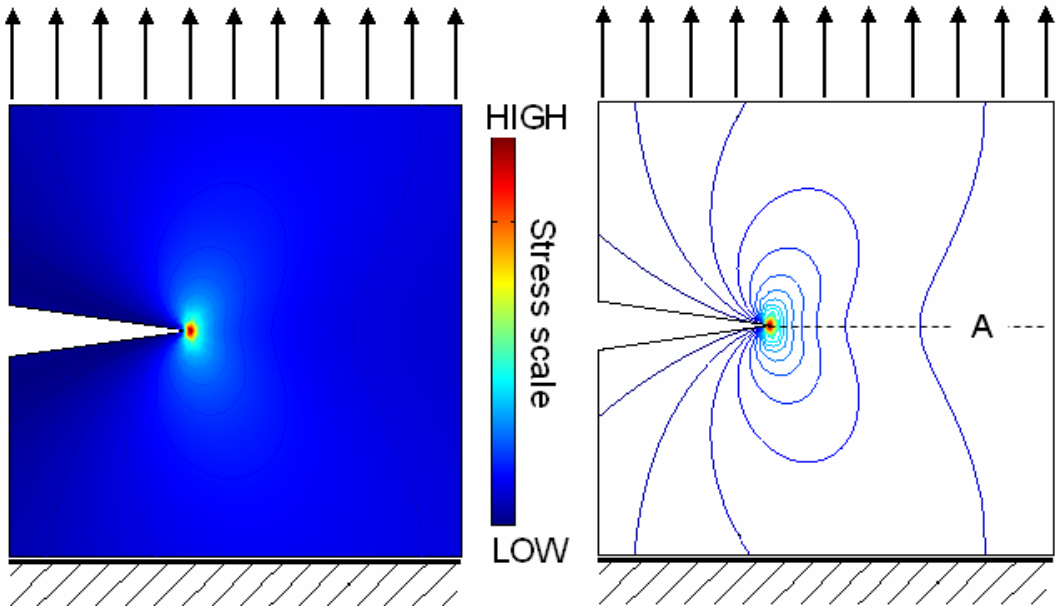

Figure 1.1: The surface (a) and contour (b) plot of the stress fields around a crack tip for a linear elastic material under plane stress uni-axial loading conditions.

is so minimal it can be considered negligible in the analysis without significantly influencing the accuracy of the results. In ductile materials a large amount of plastic deformation occurs, the effects of which can not be ignored in the failure analysis. Analysis of fracture in ductile materials is much more complex than in brittle materials due to the difficulties of accounting for the plastic deformation.

The fundamental equations of fracture mechanics are derived from energy considerations. The different approaches used to derive them will be outlined in subsequent sections. The fundamental equations of fracture are based on an energy balance between the work done by external loads and the release of strain energy compared to the increase in free surface energy resulting from the creation of new surface area and the accompanied localized plastic deformation at the crack tip (both of which are irreversible processes) [2].

1.3 History

A.A. Griffith is generally credited as the father of classical fracture mechanics due to his pioneering work during the World War I era. Prior to World War I theoretical calculations showed that the stress in the material surrounding the crack tip approached infinity as the distance from the tip decreased and resulted in a singularity at the tip of the crack, as shown by line A in Figure 1.2 . An infinite stress at the crack tip is unreasonable. If it were true, even the smallest crack would result in immediate catastrophic failure of the part because no material can withstand an infinite stress. To explain the inconsistency between the theoretical calculation and observed behavior of parts containing cracks A.A. Griffith proposed a thermodynamic approach to derive the fracture equations. Griffith's approach assumed that the energy necessary to create new crack surface came from the release of strain energy resulting from the relaxation of local stress around the crack tip as the crack advanced. Under this assumption, when the strain energy release rate becomes greater than the energy consumed by creating additional surface area the crack would become unstable and propagate across the part. The onset of unstable growth is equivalent to immediate catastrophic failure of the part. Griffth's theory approximates the strain energy release as:

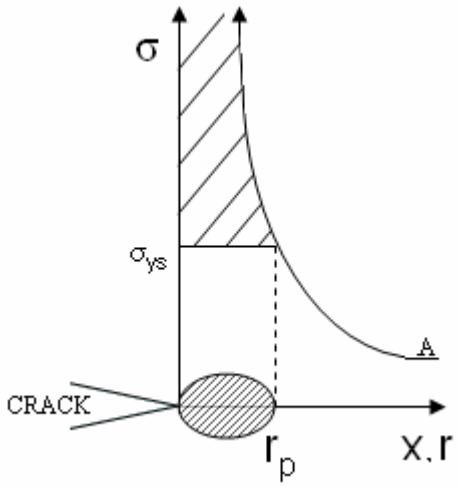

Figure 1.2: Approximate stress distribution around a crack tip [3].

$$G = \pi a \frac{\sigma^2}{E} \qquad \textbf{(1a)}$$

$$G_c = \pi a \frac{{\sigma_f}^2}{E} \quad \textbf{(1b)}$$

where G is the strain energy release rate, E is the elastic modulus, σ is the applied stress, and a is the crack length. The subscript c denotes critical and f denotes failure. When $G \geq G_c$ unstable crack growth commences.

Despite his ingenuity, Griffith's theory was generally ignored for the next two decades until World War II when Irwin and his colleagues revisited Griffith's explanation and proposed a modification. Irwin's modification replaced the term strain energy release rate (G) with stress intensity (K), and surface energy (G_c) with fracture toughness (K_c). The relationship between the separate properties is as follows:

$$K_c = \sqrt{EG_c} \text{ (plane stress)} \quad \textbf{(2a)}$$

$$K_c = \sqrt{\frac{EG_c}{1-\nu^2}} \text{ (plane strain)} \quad \textbf{(2b)}$$

where ν is Poisson's ratio [4]. The amount of strain energy available is dependent on the geometry and loading conditions of the sample.

Facture toughness is considered a material property and is defined as a materials ability to resist fracture. At the onset of failure the stress intensity (K) at the crack tip is equal to the fracture toughness (K_c) [3]. Brittle materials, such as ceramics, are characterized by low fracture toughness. Ductile materials, which include most metals, tend to be characterized by high fracture toughness [5]. Fracture toughness will be discussed in further detail in a subsequent section.

While Irwin's modification improved Griffith's theory the field of fracture mechanics was still incomplete and was limited to scenarios where the material response could be idealized as linear elastic. Please note that up until this point the entire

discussion of has been limited to the linear elastic cases and is referred to as the field of Linear Elastic Fracture Mechanics (LEFM).

Incorporating the effects of plasticity into the field of fracture mechanics took another two decades when in mid 1960's J.R. Rice introduced the J-Integral. Physically, the J-integral is the area under a load vs. displacement diagram for a given material as shown in Figure 1.3 (see also §1.5). Determining the area under the load-displacement curve is equivalent to the work (energy) per unit fracture surface area of a material[1]. The J-Integral reduces to the same equations described by LEFM under the idealized LEFM assumptions. With the introduction of the J-Integral the field of Elastic-Plastic Fracture Mechanics (EPFM) was born. Further information on the J-integral will be presented in a subsequent section.

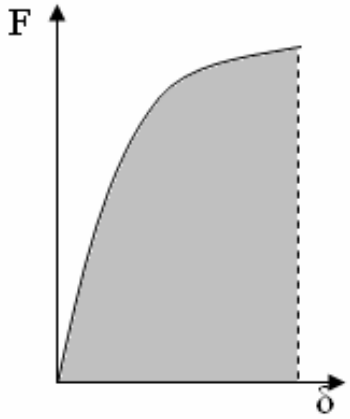

Figure 1.3: The grey region represents the value of the J-Integral [3].

The J-integral is applicable so long as the plastic deformation at the tip of the crack doesn't extend completely across the part. In the case when the plastic region extends completely across the specimen the crack tip no longer acts as a stress intensifier. When this occurs the sample is said to have succumbed to collapse. Collapse is most likely to occur in samples of materials that are thin, have a high fracture toughness, or a small crack size [3]. The stress determined for the condition of collapse is the maximum stress that can be carried by the sample, regardless of any other fracture criteria. However, it is important to remember that even when not acting as a stress intensifier, a

[1] The integral of the Load vs. Displacement curve determines the work that went into both elastically and plastically deforming the part. The elastic energy would be released during fracture and in most cases is extremely small compared to the overall energy necessary to propagate a crack.

crack is still reducing the load-bearing area of the sample, thus resulting in a higher stress for that region than in rest of the sample [6].

While the inclusion of the plasticity in a failure analysis is more complete and leads to more accurate results, it also greatly increases the complexity of the problem. The resulting increased accuracy of EPFM doesn't always justify the increased computational demands. Many 'real life' scenarios can be idealized as linear-elastic without sacrificing a great deal of accuracy. Moreover, the results of the LEFM analysis err on the conservative side by underestimating the strength and durability of a part, resulting in a larger safety factor.

Damage Mechanics provides an alternative approach for deriving the constitutive equations for fracture. Similar to Griffith's theory, the criteria for fracture in Damage Mechanics is derived from a thermodynamic approach [7]. Damage Mechanic differs from Griffth's Theory by including both time and temperature terms in the derivation of its constitutive equations. Polymers are heavily influenced by both time an temperature making Damage Mechanics a natural selection for analysis of these materials [8, 9]. The simulations conducted in this paper are not aimed at studying the effects of time and temperature so both properties will be held constant. The criteria for fracture predict by Damage Mechanics are in agreement with the criteria predicted by Griffith, Irwin, and Rice when under the same assumptions and idealizations, respectively.

1.4 Fracture Toughness and Stress Intensity

This section describes the fracture toughness (K_c) for linear elastic materials undergoing brittle fracture. A materials' ability to resist brittle fracture with a crack present is quantitatively expressed by its fracture toughness (see eq. 2a-b). It is important to note

that fracture toughness is dependent on the materials thickness. A sample under plane stress conditions, which typically occurs in thin plates, has a highly variable K_c value whereas, a thick sample under plane strain conditions, has a constant value for K_c [3, 4, 10]. The K_c values for materials presented in text books and material data sheets are assumed to be for plane strain conditions. The ASTM thickness standards for plane strain conditions under varying loading conditions and geometries can be found in the Annual ASTM Standards Books.

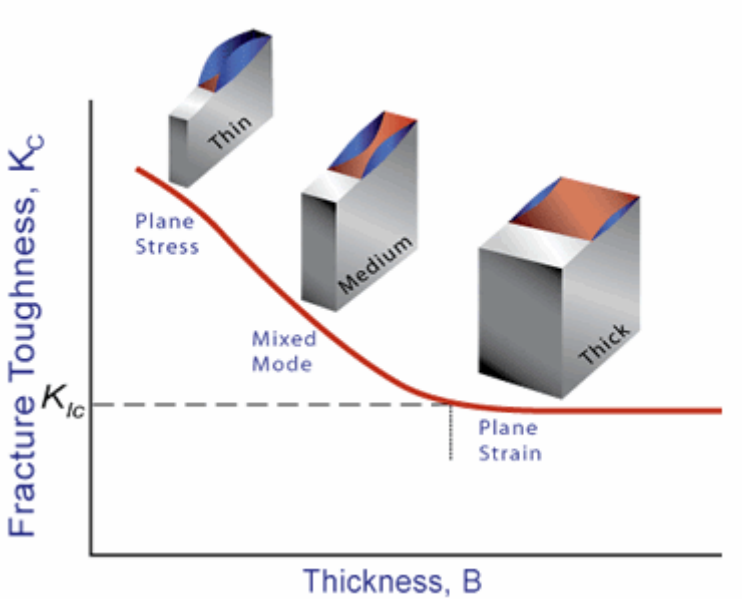

Figure 1.4: Fracture toughness is affected by thickness. The blue regions represent ductile fracture (shear lips) while the brown is brittle fracture [11].

Part of Irwin's revisions of Griffith's equations was to rewrite the strain energy density in terms of stress because a value for stress is much easier to obtain than a value for strain energy. The resulting equation is:

$$K_c = \beta \sigma_{fr} \sqrt{\pi a} \qquad \textbf{(3)}$$

where β is a geometry factor, σ_f is the stress at failure, and a is the crack length. Values for β have been determined from equations empirically fitted to the results of numerous

fracture tests of varying geometry conducted under constant loading conditions. The equations for different geometries can be found in fracture handbooks.

The stress intensity experienced by a material is dependent on the loading conditions and crack geometry. The loading conditions are broken down into thee major modes. Mode I, or crack opening, where stress is applied normal to the plane of the crack resulting in a tensile stress. Mode II, crack sliding, where the stress is acts parallel to the plane of the crack and perpendicular to the crack front creating a shear stress. Lastly Mode III, crack tearing, where the stress acts parallel to both the crack plane and front also creating a shear stress. Mode I is the most common and typically the dominant modes of failure when present [10, 12]. The different Modes of failure are shown in Figure 1.5.

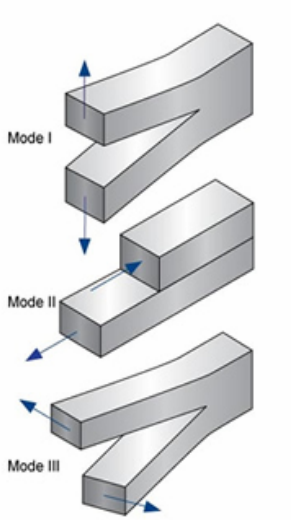

Figure 1.5: The three modes of failure [11].

1.5 The J-Integral

The J-Integral is a method used to determine the fracture criteria for cases of both LEFM and EPFM based on the conservation of energy [3, 13]. The J-Integral itself is defined by integrating the strain energy density over an arbitrary path around the crack tip. Since the contour selected for integration can be arbitrary the J-Integral is considered path-independent.

The novelty of the path independent approach is that it allows the user to select a contour far from the crack tip where the stress and strains are well-defined, bypassing the

necessity to determine the complex stress-strain states in the area immediately surrounding the crack tip. The general fracture equation for the J-Integral is:

$$J = \int_{\Gamma} \left(wdy - T\frac{\partial u}{\partial x} \right) ds \qquad \textbf{(4)}$$

where Γ is the arbitrary path of the contour around the crack, $\boldsymbol{u}$ is the displacement vector, y is the distance along the direction normal to the plane of the crack (the thickness), s is the arc length along the contour, $\boldsymbol{T}$ is the traction (or force) vector and w is the strain energy density of the material [3, 14]. Figure 1.6 helps to visualize the J-Integral.

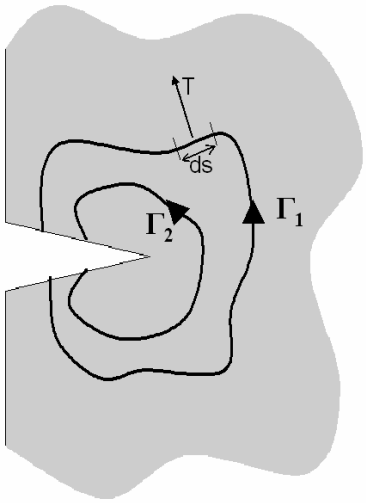

Figure 1.6: Two path-independent contours around a crack tip in an infinite plate

One of the primary difficulties inherent in the energy approach is deriving an approximate equation for the stress-strain curve to evaluate the strain energy. The Ramgood-Osborne equation is the must common method used for approximating the stress-strain equation. However, a major drawback of the non-linear approximation is its inability to mimic the unloading path followed by actual materials as shown in Figure 1.7. As a consequence of this shortcoming, EPFM can only be applied to monotonic loading situations. For the linear elastic case, the J integral reduces to the strain energy release rate G [15].

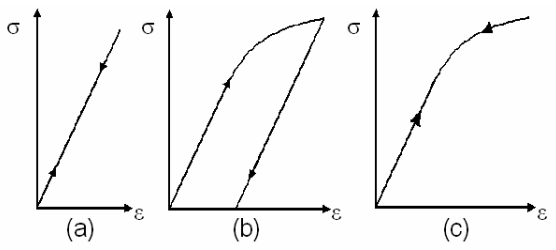

Figure 1.7: The loading and unloading paths of (a) LEFM, (b) a plastically deformed material, (c) the non-linear idealized curve that is the basis of EPFM [3]

CHAPTER 2

POLYMER COMPOSITES

2.1 Deformation of Polymers

The mechanical properties of polymers are heavily temperature dependent. However, the temperature of the simulations discussed in this paper will be held constant at approximately room temperature (~15°C, or ~60°F). This temperature is well below the polymer's glass transition temperature, assuring that the material will demonstrate the mechanical properties and deformation characteristics of a glassy polymer.

The two primary deformation mechanisms of glassy polymers at low temperatures are crazing and shear yielding. The dominant method of deformation depends on both the temperature and loading conditions. A simplified depiction of the differences between shear yielding and crazing is shown in Figure 2.1.

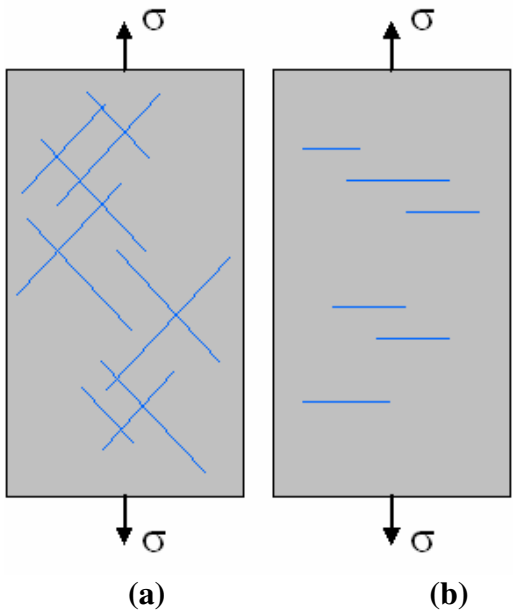

Figure 2.1: The two primary deformation mechanisms for polymers are shear bands (a) and crazes (b).

Shear yielding, or shear banding, is the flow of molecular chains or the slipping of intermolecular chains parallel to the plane of maximum shear stress (usually at a 45° angle to the tensile axis) [16]. Shear bands are initiated at stresses below the tensile strength and are accompanied by no change of volume [12].

Crazing is more favorable at lower temperatures and under positive mean pressure. Crazes form perpendicular to the axis of maximum stress and are characterized by regions of highly oriented molecules separated by porous regions as shown in Figure 2.2. The oriented molecules, or fibrils, are stronger than the general polymer matrix. However, when factoring in the porous areas the overall craze region is weaker than the surrounding polymer. The crazes also locally increase the volume and the resulting differences in volume between the crazed and uncrazed regions cause a stress concentration along the boundary. The increased stress along the boundary further propagates the craze in a direction normal to the principle stress axis. Materials that exhibit crazing generally have a higher fracture toughness than those that don't [12, 16].

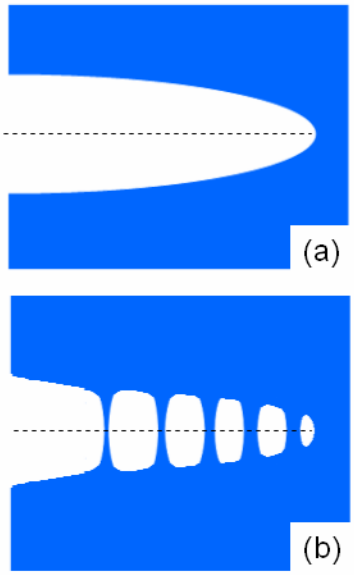

Figure 2.2: An uncrazed crack (a) and a crack with crazing near the crack tip (b).

The introduction of reinforcement elements to a polymer matrix can drastically alter the fracture toughness as well as other mechanical properties of the polymers. A great deal of research has gone into studying the effects of reinforcing polymers with microparticles and/or fibers and those results will be presented in subsequent sections. Very little research has been conducted into how the addition of both microparticles and nanoparticles could affect the properties of a polymer composite.

The intent of this thesis is to validate a multi-scale simulation technique that will allow researchers to investigate this little studied area and determine the feasibility of

creating a tough, stiff polymer composite using minimal volume fractions of particle reinforcement [17].

2.2 Fiber Reinforcement

Some of the most common composite materials are created by reinforcing a polymer matrix with fibers. These composites offer a compromise between the high stiffness and strength of the fibers and low stiffness and strength of the polymer. An added benefit of composites due to the nature of the interaction between the fiber and polymer matrix during loading is an increase in fracture toughness much higher than either of the individual components.

During fracture, fibers reinforce the polymer matrix by distributing the increased load near the crack tip over a larger area increasing the zone of plastic deformation and thus the energy dissipated. Furthermore, for a crack to propagate past the fibers the fibers must be either broken or pulled out of the matrix, both phenomena aid in the dissipation of energy, and a broken fiber can still transfer load in a polymer so long as the pieces remain longer than a critical length [12].

Fiber reinforcement is done with both long and short fibers. The fibers can be oriented in specific directions or randomly distributed throughout the matrix. The success of the fiber, or particle, reinforcement depends largely on the interfacial bonding between the polymer and reinforcement [18].

2.3 Microparticle Reinforcement

Microparticle reinforcement can have a significant impact on the mechanical properties of a polymer. In many cases a polymer can be tailored for a specific application by altering the type and volume fraction of the particle reinforcement. For polymers reinforced with a low volume fraction of microparticles, a decrease in toughness accompanied by a slight increase in stiffness has been observed [19]. On the contrary, soft micro-sized reinforcements, such as rubber particles, have been shown to substantially increase the toughness.

Toughening a polymer with soft particles enhances the permanent deformation around the crack tip, thus increasing the size of the plastic zone [20]. The modulus of the soft particles is much smaller than that of the surrounding polymer matrix. This mismatch in modulus results in three mechanism that retard crack growth. The first two mechanisms are crack tip blunting and craze promotion.

When a crack propagates into a soft particle the crack tip radius instantaneously increases to that of the soft particle. This blunting of the crack tip decreases the stress concentration at the tip of the crack. The second toughening mechanism results from soft particles in the vicinity of the crack tip. High stresses around the crack tip compress and elongate the soft particles which promotes the growth of

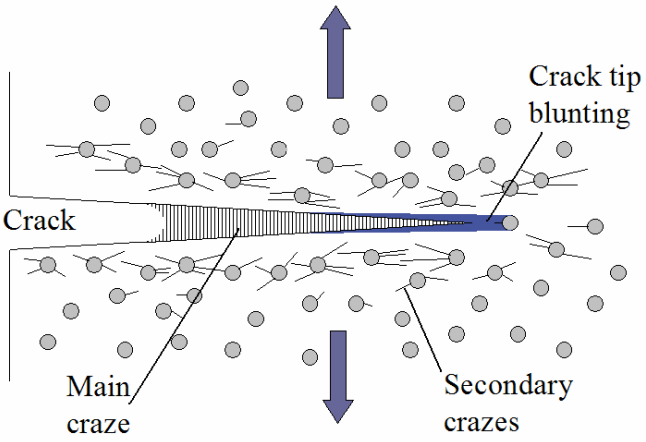

Figure 2.3: Microparticles cause crazes and crack tip blunting [12].

crazes in the polymer. Figures 2.3 illustrates the effect of crack tip blunting and craze promotion cause by soft particle reinforcement.

The third toughening mechanism is a result of the soft particles cavitating under the enormous hydrostatics stress common around the crack tip. Cavitation of the rubber particles results in a void that both increases surface area and allows room for plastic flow, which is conducive to shear yielding [21-23]. Essentially, the cavitation acts as a pressure relief valve with the particles failing prior to the polymer. Larger particles tend to cavitate first and there is a minimal radius necessary for cavitation to occur which depends on the material properties of the particle and its surface area to volume ratio. Particles with a small ratio (large diameter) have been observed to be more likely to cavitate [24, 25]. However, if the reinforcement particles are too large they can cause flaws in the matrix which weaken the polymer. Reinforcement with microparticles ranging from 0.1-10μm in diameter have been shown to yield the greatest increase in fracture toughness [21]. The side effect of toughening with soft particles is a substantial decrease in stiffness to the original polymer.

2.4 Nanoparticle Reinforcement

Nanoparticle reinforcement is another common method for altering the properties of a polymer. Nanoparticles have much larger surface area to volume ratios and as a result do not cavitate, unlike the larger microparticles. As such, the dynamics of the nanoparticle-polymer interaction are drastically different than those of the microparticle-polymer interactions.

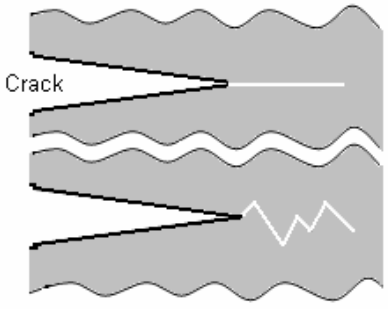

Figure 2.4: A planar crack (a) absorbs less energy than a 'jagged' crack (b).

The addition of low volume fractions of rigid nanoparticles to polymers has been shown to drastically increase the stiffness while decreasing the toughness. The embrittlement is generally attributed to nanoparticles interacting with crazes and causing them to break down forming larger voids and propagating the crack. At higher volume fractions, nanoparticles have been shown to increase the toughness through mechanisms of crack deflection and the resulting increased surface roughness/area as shown in Figure 2.4 [26]. The increased roughness results form the tortuous path of propagation necessary for the crack to avoid areas with high concentrations of reinforcement which are harder to propagate through. It can be concluded that nanoparticle toughening requires a balance between increasing plasticity without drastically increasing the damage formation in the immediate vicinity of the crack the tip [27].

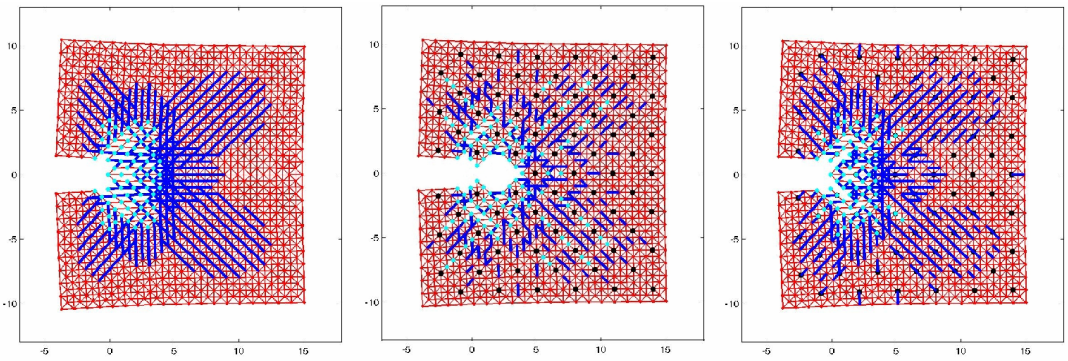

(a) **(b)** **(c)**

Figure 2.5: Molecular simulations of damage around a crack tip for an unreinforced polymer (a) and a polymer nanocomposite with nanofiller to polymer stiffness ratio 10:1 (b) and 1:10 (c). Cyan dots indicate damage zones and blue lines illustrate plastic flow [28]

The stiffness of the nanoparticle can also influence the dynamics of crack growth and the extent of damage in the polymer preceding the crack tip. Figure 2.5 shows the effects of nanoparticle stiffness on crack propagation and damage in a polymer.

2.5 Micro and Nano Reinforcement

The individual effects of microfiber, microparticle, and nanoparticle reinforcement have been thoroughly studied and the highlights have been reviewed in the previous sections. Research has also demonstrated that the synergistic mechanisms of particle and fiber reinforcement, at the micro level, can lead to both an increase in stiffness and toughness of a polymer [27].

The preceding discussion manifests the results of empirical studies which indicate that a stronger, stiffer, and tougher polymer could be realized through micro and nanoparticle reinforcement. Accurate models that can simulate the interactions between the microparticles, nanoparticles, and polymer would give insight into how and why this method of reinforcement is effective. These models can then be used to facilitate parameter studies and minimize the fabrication and testing required for validating specific phenomenon.

CHAPTER 3

COMPUTATIONAL FRACTURE MECHANICS

3.1 Challenges of modeling crack propagation.

The challenges that arise when modeling crack initiation and propagation can be subdivided into the following categories: material, mechanical, geometric, and transitional. During crack nucleation and propagation both elastic and plastic deformation occurs in the material. Modeling the elastic-plastic deformation results in a nonlinear idealization of the material's stress-strain curve. The idealized curve does not accurately represent the unloading of the material in the simulation (as discussed previously) and increases the computational complexity of the simulation [29].

The mechanical requirements, often referred to as the relevant crack growth parameters, are extracted from a stress analysis of the model and used to determine the crack extension, growth direction, and shape. Stress intensity or energy considerations are the primary properties used to determine the crack growth parameters [30]. Additional complications can arise during non-planar crack growth when the opening and closing of the crack results in contact between the crack surfaces and causes mixed-mode fracture.

The geometry of the model also changes as the crack propagates. The change in geometry must be accounted for in order to accurately evaluate the mechanical requirements listed above. A new stress analysis must be performed for each incremental crack step to update the crack growth parameters. Depending on the method used to simulate the crack propagation updating the stress field may, or may not, require re-meshing the model.

Lastly, most methods for evaluating crack propagation require a number of different length scales. A macro-scale analysis can be conducted on the majority of the part but the key area of interest, the area around the crack, must be evaluated at a micro- or nano-scale to more accurately simulate the crack growth. The transition in the model from larger to smaller length scales must be seamless in order to ensure the continuity of the model [30].

The methods used to evaluate the models at different length scales must also be taken into consideration. Continuum theory is not expected to be valid as the length scale of the analysis approaches that of the radius of gyration of the polymer. The radius of gyration is statistically defined as the root mean squared distance between the centroid of the polymer chain and each of its monomers [32]. The average polymer chain length for a material similar to that used in the simulations presented in this paper (similar to Nylon 6,6) is expected to be approximately .5-1.5 μm. The chains, which are composed of the mers presented in Figure 3.1, are expected to assume a random coil configuration with outer dimensions scaling with the square root of the number of monomers in the chain [33]. The resulting radius of gyration would be approximately 100 nm. Therefore the constitutive equations that govern the FEA will not be applicable at the very tip of the crack, which is an area of specific interest in this paper [34]. The novelty of the modeling

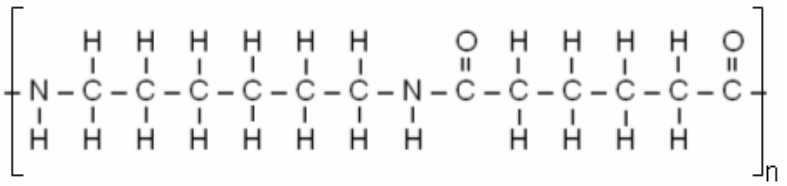

Figure 3.1: A Nylon 6,6 mer. The degree of polymerization is expected to be ~420, resulting in an average chain length of ~905 nm and a radius of gyration of ~30 nm [31].

approach discussed in this paper lies in the implementation of a Normal Mode Analysis in the immediate vicinity of the crack tip in place of the invalid FEA.

3.2 Basic Modeling Procedure

Crack analysis is an incremental process that starts with a representation of the model which includes: the geometry, boundary conditions, initial cracks and material properties. The representational state is then discretized by a mesh. The discretized model

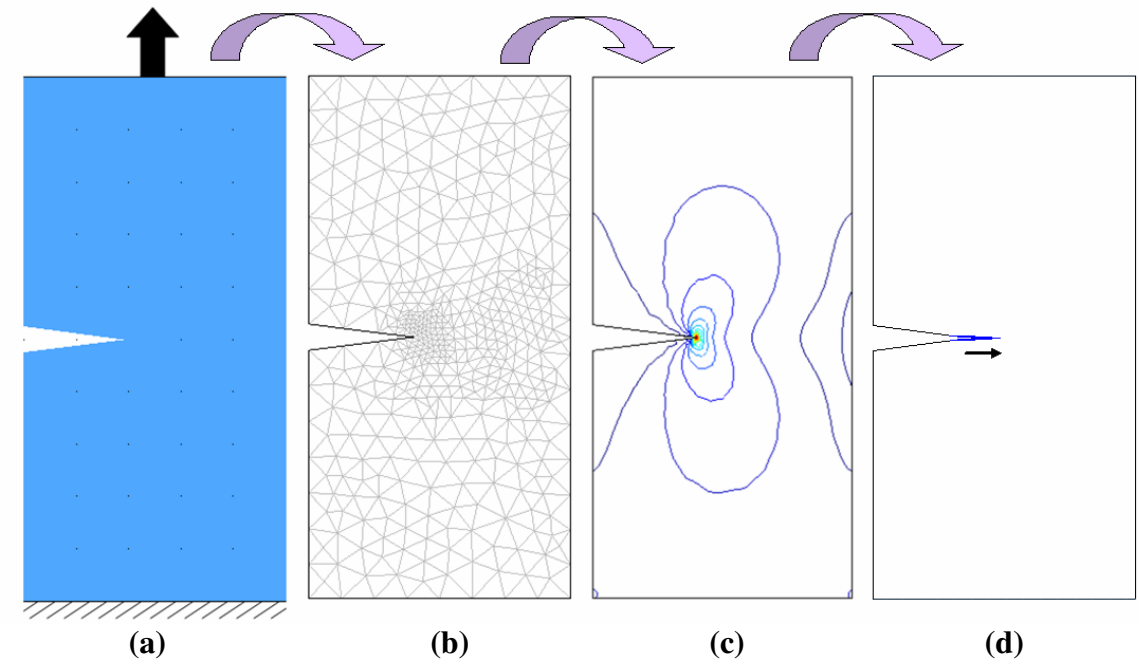

Figure 3.2: The progression of crack propagation simulation: The model geometry and boundary conditions are defined (a), the model is then discretized (b) and solved (c). Crack growth and direction is determined from relevant fracture parameters (d). The original model would then be updated to reflect changes.

can then be evaluated by a solver. The solver performs the stress analysis from which an equilibrium database is created and the relevant fracture parameters are gleaned. The equilibrium parameters include such variables as stress and displacement while the fracture parameters commonly include stress intensity or energy considerations that are necessary to determine crack growth and direction. The original representational model is

then updated to reflect the changes incurred by the crack growth. Figure 3.2 shows a diagram of the process [35-38]

3.3 Methods for Modeling Crack Propagation

There are a variety of different methods used to analyze crack propagation including boundary representation (B-Rep), finite-difference, finite-element (FEM), and a host of meshless methods including the element-free Galerkin method (which differs from FEM by replacing the mesh by nodes with weight functions [39]) and the Lattice-Spring Models (LSM) sometimes referred to as Elastic Network Models (ENM) [37]. As a result of the complexity of crack propagation many of the methods require oversimplification of the crack details in order to conduct an analysis. The oversimplification leads to inaccurate results. However, two methods, FEMs and the ENMs, have proven to be the most versatile and accurate over a wide variety of conditions.

There are a variety of commercial FEM modeling packages on the market, the most prominent being ANSYS, ProE, Solid Works, and COMSOL. The commercial packages are all inclusive, coming with all the necessary applications to create, apply loads to, mesh, and analyze a model. The software selected for the FEM modeling discussed in this paper was COMSOL. COMSOL was selected because of its versatility, accuracy, user friendly graphic user interface, and its scripting application which easily interfaces with MATLAB. The ENM that will be used to evaluate the region around the crack tip is a MATLAB program created by Professor Moon Kim. This particular ENM uses a Normal Mode Analysis (NMA) to solve the potential functions governing the dynamics of the system and determine the displacement and direction of the nodes

comprising the network. More information on COMSOL and the ENM will be presented in ensuing sections.

3.4 Finite-Element Methods

FEM programs are most commonly used to evaluate the stress fields present in parts and assemblies under given equilibrium and loading conditions. These programs reduce the partial differential equations governing the underlying physics of the model into a series of polynomials that can than be evaluate at discrete points defined by the mesh [40]. Therefore, the accuracy of these models is heavily dependent on the mesh applied to the model. The mesh needs to be fine in order to minimize the error incurred by extrapolating data between nodes. Unfortunately, a fine mesh takes more memory to create and analyze thus increasing the computational cost of the analysis. Also, in some case the mesh size could be scaled smaller than the lower limits of continuum mechanics. At this scale the basic assumptions on which the governing constitutive equations are based, are no longer valid. At the other end of the spectrum a coarser mesh acquires greater error by increasing the range of extrapolation between nodes. The advantage of the larger meshes is that they can be evaluated much quicker than the finer meshes.

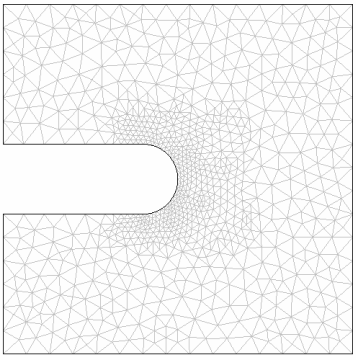

Figure 3.3: A block with a mesh gradient.

Striking a balance between a fine and coarse mesh is imperative for obtaining accurate results in a timely manner. In many cases a mesh gradient can be implemented, as shown in Figure 3.3 allowing a finer mesh to be located in more critical regions, such as around a stress concentration, and a coarser mesh in more

stable regions. The simulations in this paper will use a mesh gradient similar to the one shown in Figure 3.3.

While most FEM programs are capable of performing a nonlinear analysis of a part with elastic-plastic material properties it's very uncommon for them have the ability to simulate crack initiation and growth. An extremely fine mesh in the vicinity of the crack tip is necessary to allow the crack to propagate along an arbitrary path. The fine mesh must also be reapplied to the model after each incremental crack step. The computational cost of solving and reapplying the mesh is exorbitant and is the primary reason commercial FEMs don't model fracture [29, 36]. However, updating the original geometry after the crack growth is also a difficult process.

There are a few independent software applications that have been created to work in conjunction with the commercial solvers to simulate crack growth. The most prominent of these is FRANC3D, a 3D FRacture ANalysis Code, created by the Cornell Fracture Group. FRANC3D automates the discretization and update process necessary to model crack propagation [37]. FRANC3D has demonstrated accuracy in modeling cracks as complex as 3D non-planar and is available as a free download from the Cornell Fracture Group's website[42, 43]. FRANC3D is limited to isotropic materials with known bulk characteristics and does not account for non continuum behavior below the limits of continuum mechanics. Although FRANC3D is not used for any of the simulations presented in this paper the concept of its methods and processes are very similar to what is hoped to be accomplished in this research.

3.5 Overview of Elastic Network Models

A typical ENM is composed of a 2D or 3D arrangement of 1D springs where the

atoms or particles are represented by the nodes, and the springs represent the bonding force between the atoms or particles [44]. ENMs are considered meshless because the nodes are not resultant from a mesh. By patching nodes instead of a mesh around a crack the model doesn't have to be re-meshed after each increment of crack propagation, which greatly reduces the simulation's computational demand. An example of a network that could compose an ENM is shown in Figure 3.4.

ENMs can be used to model all the atoms in a system, however, as the size of the system increases this approach becomes inefficient and too computationally costly to be conducted on anything less than a super computer [45, 46]. To mitigate the computational demands coarse-grained ENM have been developed. Coarse-grained ENMs simplify the analysis by only modeling a part of the structure being studied. For example only the alpha C atoms in a protein structure or just the carbon amides in a polymers' chain would be assigned as point masses and connected by the springs. Comparing the results of coarse grained ENMs to those of all-atom systems and experimental findings have shown them to be sufficiently reasonable and accurate for predicting the overall dynamics of the system [47].

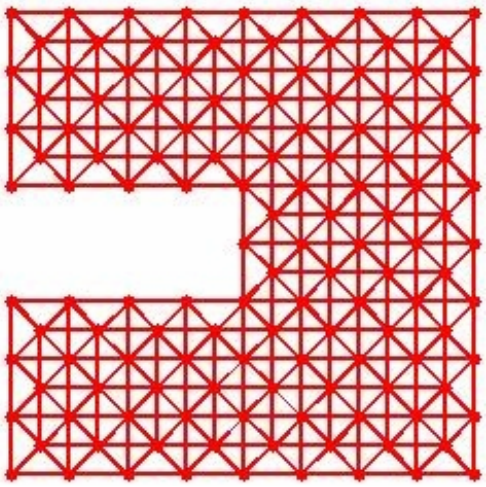

Figure 3.4: An example of the network of nodes and springs composing an ENM [28].

Once the nodes in the network have been designated the virtual springs must be applied to account for the interactions between atoms/molecules. There are two

predominant methods for determine how and where the springs will be applied, they are the distance cut-off and chemical bond method. The distance cut-off method connects a node to all the other nodes within a certain proximity of it. Selecting an inappropriate cut-off distance will result in an over or under representation of the global stiffness by incorrectly accounting for the interactions between nodes. The resulting model will be unstable and inaccurate [46, 48].

The chemical bond method reduces the degrees of freedom of the system by connecting four consecutive particles that compose the backbone of the structure. The randomly applied bond length, angle, and direction limit the degrees of freedom of the model. This procedure stabilizes the elastic network resulting in more accurate and robust solutions [46].

The values of the virtual springs must then be selected to accurately depict the different bond forces found in the system being modeled. For polymers that means there will be different spring values to represent both the primary (covalent) bonds along the polymer's backbone and weaker secondary (hydrogen and Van der Waals) bonds between the different polymer chains [49].

ENMs are also able to model elastic-plastic material properties that would be found around the tip of a crack by altering the spring constants to account for the nonlinear effect of plasticity and ultimately breaking after a certain elongation. Similarly in a heterogeneous material, such as a nano-reinforced polymer, the interface between the particle and polymer matrix can be adjusted by altering the spring constant between the nodes representing the matrix and those representing the reinforcement particles. In the

case of the reinforced polymer, a Monte Carlo simulation would then be performed to equilibrate the model [50].

However, some ENM simulations of plastic deformation have concluded with Poisson's ratios of less than .5 in areas of plastic deformation indicating a failure conserve volume and casting some doubts on the validity of the model [51]. Another drawback to ENMs are occasional stress anomalies that occur along particle surfaces. These errors can be minimized by altering the spring constants representing the interfacial bonds [50].

Once an ENM is set up the equations governing the dynamics of the system must be assigned and solved. The most common method for solving the system of equations is NMA. NMA approximates the empirically prescribed potential functions as harmonic functions and analyzes the lowest mode frequencies which are most suitable for describing the global motion of the system [45, 46]. The drawback to NMA lies in its inability to account for anharmonic motion and highly detailed atomic motion (a result of evaluating only the low frequency modes) [45]. The specific ENM used in this research will be discussed in greater detail in a later section.

3.6 COMSOL Multiphysics and the ENM

This section gives a more in-depth perspective of how the programs selected for this research will be set-up to accomplish their specific tasks.

3.6.1 COMSOL Multiphysics v3.3

COMSOL Multiphysics performs equation-based multiphysics modeling with a user-friendly interface [52]. COMSOL offers a variety of modules that facilitate the

analysis of specific scientific and engineering phenomenon. The 2D Plane Stress Structural Mechanics module was utilized for this research. Recall that the plane stress condition dictates that σ_z, τ_{yz}, and τ_{xz} are assumed to be zero in the stress tensor. The 2D model allows for loads in the *x* and *y* direction and assumes that these loads are constant through the thickness.

3.6.2 The Elastic Network Model

The ENM used in the simulations presented in this thesis will use the cut-off distance method to determine how the springs will be applied between each node. Only structural information will be used to define the potential functions governing the system dynamics [53]. A NMA will be used to solve the constitutive equations of the system and the corresponding direction and displacement for each node in the network will be obtained from the eigenvectors and eigenvalues, respectively, resulting from the solution [17].

The ENM aspect of this research will follow these iterative steps: i) the initial model will be created in an equilibrated state ii) NMA will be applied to find a few of the slowest modes, iii) perturb the initial conformation by adding a scaled slowest mode, iv) evaluate the plastic flow and the damage zone by measuring the change in spring lengths, v) rebuild the elastic network for the deformed conformation, and vi) back to step ii) and repeat the preceding procedure [17].

To model a nano reinforced polymer a portion of the nodes in the lattice spring network will be replaced by the nanoparticles and the spring values connecting them to surrounding nodes, as well as their sphere of influence will be adjusted accordingly.

3.6.3 Integrating COMSOL and the ENM

A seamless interface between COMSOL and the ENM was necessary to ensure accurate and realistic results. The ENM was responsible for modeling the material within a half micron around the crack tip. The large ENM patch size assured the patch boundaries fell within the region where continuum mechanics is applicable. This ensured the results from the FEA of outer portion of the model were valid and also allows the results of the coupled schemes to be compared to the results of a full FEA of the same geometry.

The COMSOL and ENM simulations were performed discretely. Each aspect of the simulation was run to convergence before passing data to the next step. This process was than iterated five times, which was sufficient for all models to converge.

The modeling process began with the part's geometry being created in COMSOL. Boundary conditions were applied and the part was meshed. For the initial iteration the patch boundaries were fully confined by setting the allowable displacement equal to 0 in all directions. COMSOL then determined the stress and displacement conditions that existed throughout the model.

The force along the patch boundary was than output to the ENM. An interpolation function, internal to COMSOL, was used to determine the force values for the ENM nodes that did not coincide with an element vertex from the COMSOL mesh.

The ENM then computed the nodal displacements and directions, both along the boundary and throughout the network, from the applied boundary forces. Ultimately the nodal displacements would be compared to a stop criterion (such the percent change in outputs between successive iterations) to determine if the simulation would continue or

stop. [17]. For the simulations presented in this research the number of iterations was set to six. An overview of the simulation process can be seen in Figure 3.5.

From the perspective of COMSOL, the ENM looks like a complex user defined constitutive stress-strain relation. Fortunately COMSOL was designed to interface with MATLAB and the ENM was written as a MATLAB file. The mutual affiliation to MATLAB shared by both COMSOL and ENM eased the "handshaking" between models.

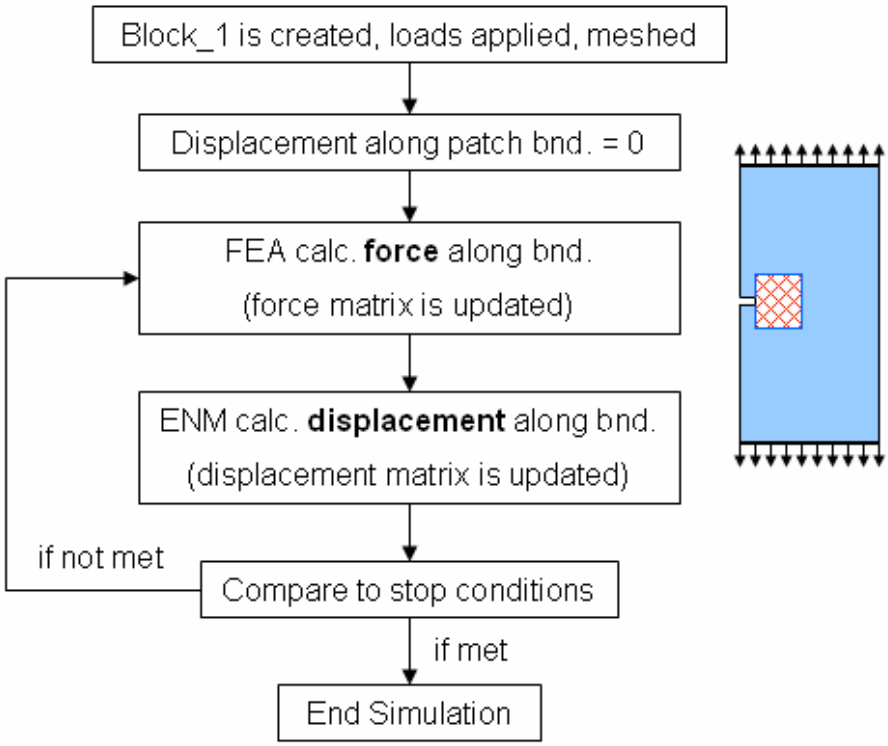

Figure 3.5: Flow chart of the multi-scale modeling process.

CHAPTER 4

IMPLEMENTATION OF HYBRID ENM-FEA MODELS

The intent of this research was to determine the feasibility and limitations of an ENM-FEA coupled analysis scheme by analyzing the simulation results of increasingly complex models. Validation of the ENM-FEA scheme was tested by comparing the outputs along the patch boundary of the ENM-FEA simulation to those of a FEA-FEA and single-region FEA simulation.

The majority of the models studied did not have cracks present in their geometries. Therefore the results from the single-region FEA were an accurate benchmark to compare the results of the coupled simulations. Results from the single-region FEA evaluation of cracked geometries were expected to be accurate in regions far from the crack tip and were still used as benchmarks for the coupled analysis schemes. In all cases the results of the FEA-FEA closely followed those of the ENM-FEA scheme but the FEA-FEA scheme took less than a minute to complete most simulations while the ENM-FEA scheme took over an hour (based on a five iteration simulation). As a result of the time disparity it was advantageous to run the FEA-FEA scheme prior to the ENM-FEA scheme to initially explore new scenarios and resolve any potential problems with data exchange between models (coupling) or boundary conditions.

Over all, the two coupled analysis schemes were used to analyze models with two different material properties, under three different external loading conditions, and six different geometries. An overview as well as an explanation for the analysis schemes,

material property, and external loading selection process will be presented in this chapter. The model geometries will be discussed in subsequent chapters.

4.1 Analysis Schemes

All of the models can be broken up into two parts; an outer region and a patch region. The outer region was where the external loads were applied and was always analyzed using FEA. Internal loads were transferred to the patch region which was evaluated by either FEA or ENM. This led to two coupled analysis schemes: FEA-FEA and ENM-FEA.

Regions evaluated by FEA required a mesh. The element size along the boundary between the outer and the patch region was confined to 50nm. An unconstrained free mesh, constructed by the FEA software, was implemented in the remainder of the subdomain. An approximation of the mesh can be seen in Figure 4.1. A mapped mesh could have been implemented, and was in preliminary research, but applying a mapped mesh became cumbersome after the introduction of the necessary point constraints to prevent rigid body motion in later models. Results between models analyzed with both free and mapped meshes were indistinguishable.

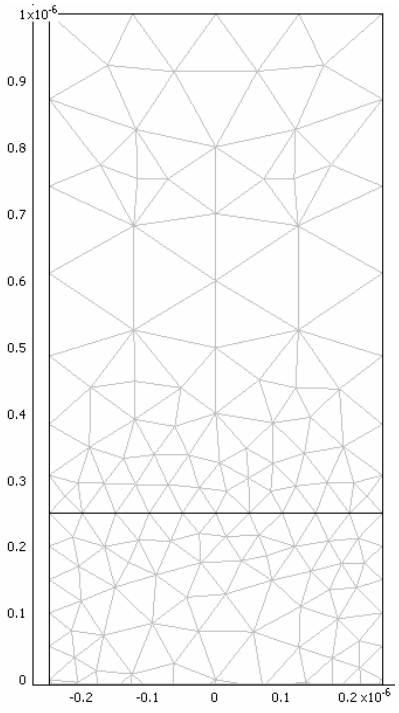

Figure 4.1: Mesh gradient in the stick model.

Regardless of the analysis scheme (FEA-FEA or ENM-FEA) the order of data transfer across patch boundaries was consistent. The outer-region was analyzed first with

an external load applied to the top and bottom boundaries and zero displacement inputs in all directions applied at the patch boundaries. Forces both normal and tangential to the patch boundaries resulted from the imposed displacement conditions. The normal forces were then transferred to the patch model. The patch was analyzed and the resulting normal displacements were exported to the outer region.

It was not necessary to exchange the tangential data between boundaries because the sum of the tangential data along a boundary is represented by the normal force vector on the boundary perpendicular to the original boundary, as shown in Figure 4.2. During the analysis the normal force scalar from the perpendicular boundary (F_2) is incremented over the length of the boundary (top row) in order to best satisfy the internally prescribed equilibrium conditions. Preliminary simulations confirmed that excluding the tangential data had negligible effects on the results.

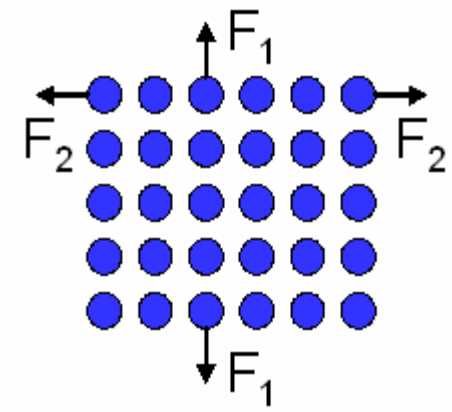

Figure 4.2: F_2 is distributed through the top row the same way F_1 is distributed through the third column.

Iterations were expected for the coupled analysis schemes to converge. The iterations were necessary as a result of the unnatural zero displacement constraint initially applied to the interfacial boundaries in the coupled analysis. These imposed boundary conditions caused stress concentrations in the vicinity of the boundaries that resulted in force outputs that were larger than what would have been observed in a model without the overconstrained boundary (like the single-region FEA model). The higher forces were transferred to the ENM and caused larger displacements than predicted by the single-

region model. The large displacements compressed the outer region and the subsequent force outputs were negative causing smaller than expected displacement outputs and continuing the cycle until eventual reaching an equilibrium state in which outputs from consecutive iterations were the same. Conditioning the data exchanged between the coupled models expedited convergence. Details of the data conditioning algorithms will be presented in §5.3.1 and §5.3.2.

Convergence was determined by comparing the displacement outputs of consecutive iterations. If the average absolute value of the percent error between the final two iterations was less than 1.0% percent, the model was considered to have converged. The convergence was based on the displacement outputs because they were not conditioned at any point in the simulation. In all cases the force convergence was better than the displacement convergence.

Accuracy of the simulation was determined by comparing the displacement values from the final iteration to either an analytical solution, when available, or the single-region FEA analysis of the same model. When the average absolute value of the percent error of the final FEA-FEA simulation was less than 2.0% of the solutions', the model was considered to be accurate. The ENM-FEA results where compared both to the overall solution as well as the FEA-FEA solution to determine an absolute and relative accuracy, respectively. Accurate ENM-FEA results were considered to be within 0.20%[2] percent of the FEA-FEA model. This implies converged within 2.2% percent of the actual solution. In all cases an absolute accuracy implied relative accuracy as well (the ENM-FEA results were never better than the FEA-FEA results).

[2] This value was determined by comparing the displacement results of the patch region, under the same loading condition, from an FEA and ENM analysis. The average deviation between results of the two methods was 0.20%.

No algorithm was applied to stop the iterations when the models had reached a set convergence value. Instead, each simulation was run for a total of five iterations. All of the models were able to converge in fewer than five iterations; the additional iterations after convergence were a test of the models numerical stability and also gave further insight into convergence characteristics between successive iterations in the coupled schemes.

4.2 Material Property Selection and Validation

One of the eventual applications of the coupled ENM-FEA modeling scheme is to analyze nanoreinforced polymers which can be both isotropic and anisotropic. The material properties used for the isotropic and anisotropic models were selected to represent generic isotropic and anisotropic polymer material properties, not a specific material. The method used to determine the exact material properties used in the research is described in the subsequent paragraph.

The first step was to determine a range of acceptable values for the modulus of elasticity and Poisson's ratio for both the isotropic and anisotropic materials. Poisson's ratio was set to 0.3 and the upper and lower limits of the elastic modulus were applied to the patch region. The patch region was than analyzed by the FEA software (after applying an external load). The displacements results of the analysis were recorded for later use.

The patch region (subjected to the same external loading conditions) was than analyzed with the ENM. The spring constants of the ENM were altered until the displacement output fell within the range established by the previously mentioned FEA.

The material properties of the FEA were then adjusted so the displacement outputs from both analysis's (FEA and ENM) of the patch were as close as possible.

The final values selected for the elastic modulus and the Poisson's ratio for the isotropic case were 168.5 GPa and 0.496, respectively. Poisson's ratio for the ENM was a consequence of the spring stiffness and connection characteristics implemented in the model; a numerical value could not be explicitly assigned. In future models the value of the spring stiffness, as well as how the springs connect the nodes can be altered to result in a more realistic Poisson's ratio. For the anisotropic case the elastic modulus in the y direction was 146.5 GPa and the modulus in the x and z direction was 73.3 GPa. A Poisson's ratio of 0.3 was used in all directions for the anisotropic case.

Equivalent material characteristics for the isotropic case in the ENM were obtained by setting all spring constants equal to 100/91 [N/m]. For the anisotropic case the vertical spring constants remained 100/91 [N/m] while both the diagonal and horizontal spring constants were set to 50/91 [N/m].

Displacement results for the patch region under uniaxial external loading (0.001 [N/m] force/length applied to top and bottom boundary) for the isotropic case are shown in Figure 4.3. The ENM displaces on average 0.20% more than the FEA results and almost 2.0% more at the corners. Results of the anisotropic case were similar.

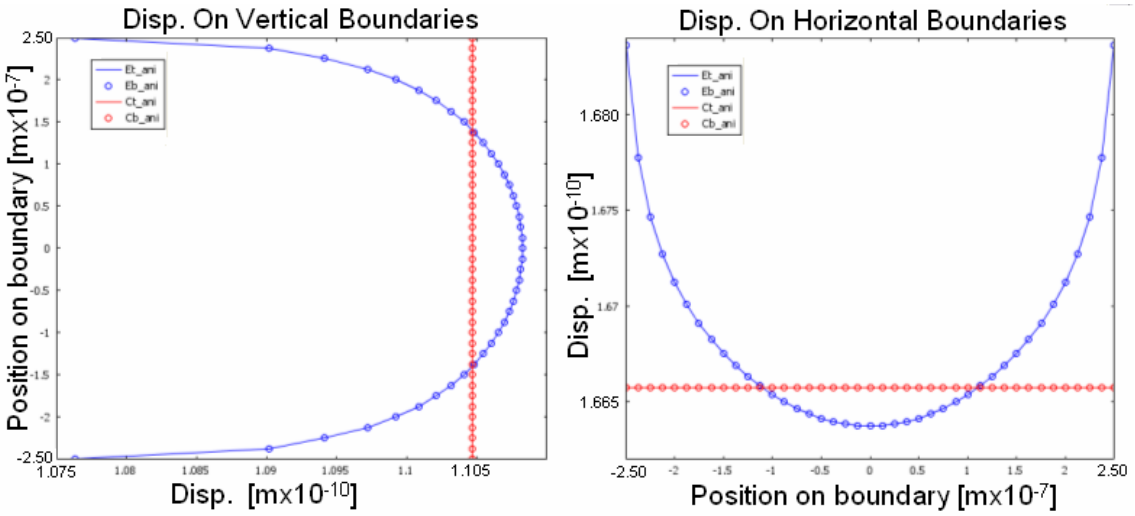

Figure 4.3: Displacement results of FEA (red) and ENM (blue) analysis of the patch region under a uniaxial load. The top, bottom, right and left boundaries are denoted in this and all subsequent legends as 't', 'b', 'r', and 'l', respectively.

The patch was also validated for a biaxial external loading case (same as uniaxial with 0.0003 N/m force/length applied to side boundaries). The results of both the anisotropic and isotropic case looked similar; displacements from the isotropic case are shown in Figure 4.4. The top and bottom boundaries under biaxial loading displaced on average 0.10% with a maximum deviation of 1.0% at the corners. The better accuracy obtained from the biaxial loading case was attributed to the compressive forces applied to the sides of the patch which would reduce the over extension of the corner node by effectively pulling it in.

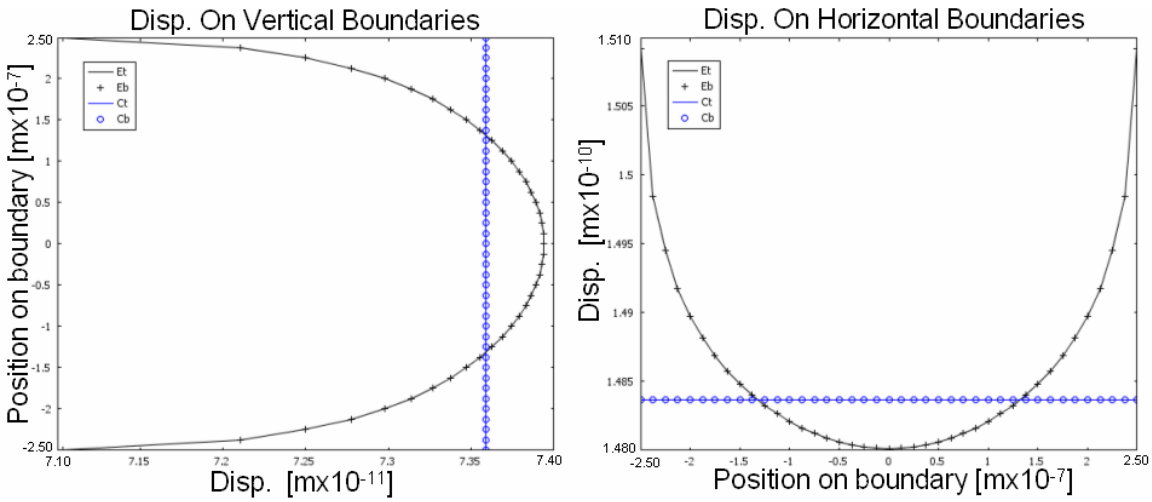

Figure 4.4: Displacement results of FEA (blue) and ENM (black) analysis of the patch region under a biaxial load.

In all case the displacement outputs of the ENM are curved while the displacement outputs of the FEA appear constant thought the length of the boundary. The parabolic nature of the ENM output is a result of the lack of springs connecting the outer row of nodes to the rest of the ENM. The majority of the nodes in the ENM have eight springs connecting them to their neighbor nodes. Nodes along the ENM edge have only five springs, and the corners have only three, as shown in Figure 4.5. The lack of springs results in decreased stiffness, and explains the increased displacement experienced by the ENM, which is particularly noticeable at the corners.

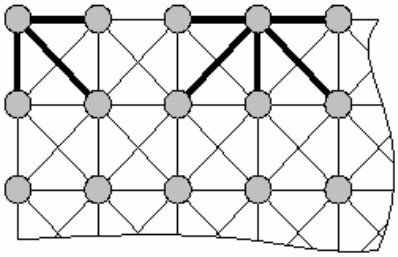

Figure 4.5: Close up of corner and boundary nodes in ENM.

The parabolic nature of the ENM outputs is diminished by two phenomena during the coupled schemes. Physically, the patch is located in the middle of a block in the coupled schemes. The material surrounding the patch acts as an added constraint to the ENM model and would prevent the corners from displacing as much and correct it over subsequent iterations.

In an effort to limit the displacement of the corner nodes in the ENM a uniform uniaxial load was applied to the first row into the ENM from the second to second to last column. The patch was evaluated and the results were compared to those of the patch under 'normal' uniaxial loading (force applied along the top row). This technique did nothing to lessen the exaggerated displacement of the corner nodes.

Ultimately, a cutoff algorithm was also used to limit the displacement of the corners in the initial iteration (which was unaffected by the surrounding material) to accelerate convergence. More detail on this algorithm is given in §5.3.1.

4.3 External Loading Conditions

Three different loading conditions, all tensile, were applied to the models. Tensile loads, as opposed to compressive loads, were selected because they are more conducive to crack growth. The first loading case (a) was a uniform 0.001 N/m. The second case (b) was non-uniform but symmetric with respect to the y axis and varied in magnitude from 0.001 N/m to 0.0006 N/m. The third case (c) linearly decreased in magnitude from 0.001 N/m to 0.0005 N/m. In all cases the load was applied along the top and bottom boundary. The loading cases are shown in Figure 4.6.

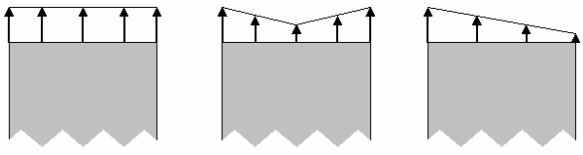

Figure 4.6: Loading Conditions

The uniform loading case was applied to all the models. The non-uniform cases were only applied to models without a crack included in the geometry. The non-uniform loading cases were applied to the uncracked model to determine how the coupled analysis schemes would handle nonuniform loads across the patch boundary. The presence of cracks in any of the model's geometry would also result

in non-uniform loads across the patch boundaries. Observing the effects of the non-uniform loading conditions, without having to consider the complexities cause by a crack tip, represented a controlled step in the progressively complex modeling method.

The uniform force per length of 0.001 N/m was selected because it resulted in a 100 MPa stress throughout the un-cracked geometries. This stress falls within the elastic region (which is where FEA is valid) for most materials, including the isotropic and anisotropic models used in this research. The applied force/length still caused unrealistic stress values at crack tips (for models containing cracks in their geometry) when evaluated with FEA. The inflated stress values were expected, but their effect was localized to within a small vicinity of the crack tip and the stress field had fully relaxed to reasonable values well within the limits of the patch region. This observation is important because it indicates the force and displacement outputs at the patch boundaries are unaffected by the exaggerated stresses of the crack tip and therefore like models evaluated by different schemes can be compared both to each other and to the solution model which was evaluated only by FEA.

The coupled analysis schemes were applied to a variety of geometries and loading conditions. These model variations will be presented in subsequent chapters.

CHAPTER 5

ANALYSIS OF A TWO-SIDED TRANSVERSE INTERFACE MODEL

5.1 Model Description

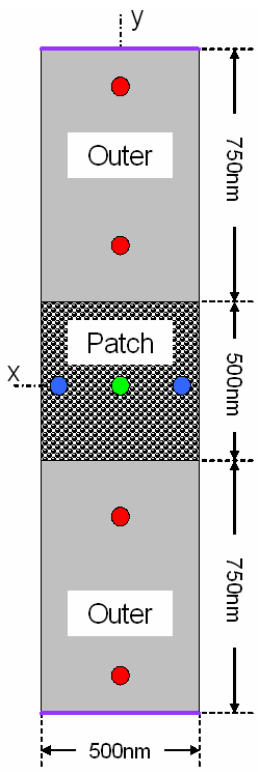

Figure 5.1: The stick geometry.

The two-sided transverse interface model is a 2000x500nm rectangle, with a 500x500nm patch in the middle. Due to the stick-like nature of the model, the two-sided transverse interface model will henceforth be referred to as the 'stick' model. The thickness of the stick model, as well as the thickness for all the models studied in this research, was set to 0.01 nm. Dimensions of the stick are shown in Figure 5.1. Rigid body motion was prevented by applying point constraints to the model. In Figure 5.1 the red dots indicate points with fixed x displacements and blue dots indicate fixed y displacements. The green dot in the middle of the patch region is constrained in both the x and y direction. The constraints were located along the axes of symmetry for loading cases (a) and (b) and close enough to the axis of symmetry in loading case (c) such that their effect on the outcome was minimal. The external loading was applied along the top and bottom edge of the outer region (purple lines). Figure 5.2 shows the modeling tree for the stick geometry.

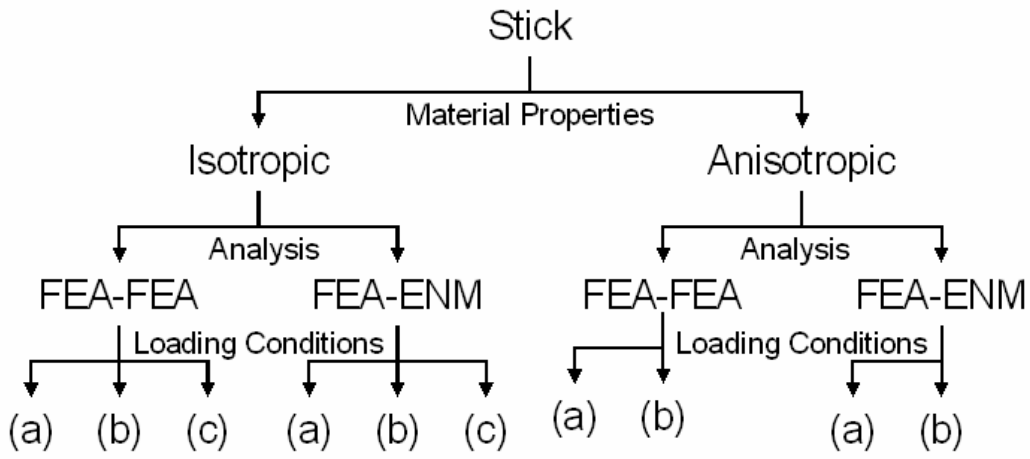

Figure 5.2: Modeling Tree for the stick geometry; (a), (b) and (c) refer to the loading cases shown in Figure 4.5 (10 total models).

5.2 Objective

The objective of the stick model was to explore the possibility of coupled analysis schemes and determine the necessary steps for convergence. In all cases the FEA-FEA scheme was tested first, to verify interface conditions, followed by the ENM-FEA. The initial analysis was of the stick subjected to the uniform loading condition with isotropic material properties. After the model was shown to converge non-uniform loads were applied to the stick to see if the analysis schemes could handle crack like conditions. This procedure was then repeated for the anisotropic case.

5.3 FEA-FEA: Uniform Load with Isotropic Properties

The force and displacement results along the horizontal boundaries of the stick model under a uniform load with isotropic material properties are shown in Figure 5.3. The iterations in Figure 5.3, and for all the Figures in this section, are denoted by the blue, red, green, yellow, and cyan lines, for the first through fifth iteration, respectively. The black line indicates the solution. The force and displacement outputs of the analysis

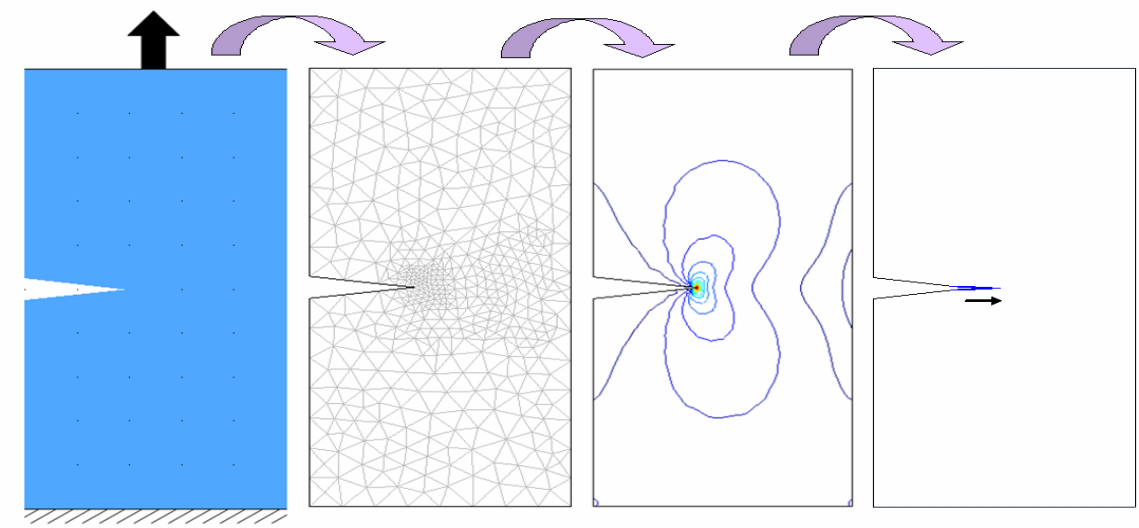

Figure 5.3: Simulation results for six iterations of a FEA-FEA coupled analysis with both relaxation and cut-off algorithms applied.

were accurate with respect to the expected solution to within 0.37%, on average. The change in value between the last and second to last iteration was, on average, less than 0.36%. Both of these values are well within the limits of convergence and accuracy defined in §4.1. The percentage error in displacement of each individual node with respect to its corresponding solution node can be seen in Figure 5.4. From the initial investigation it was determined that both a cutoff and relaxation algorithm were necessary for convergence. The cutoff algorithm was needed for the FEA to evaluate the patch and outer region during the first iteration. The relaxation algorithm expedited the convergence by dampening the oscillations of the iterative systems. A detailed description of both these algorithms is presented in the following sections.

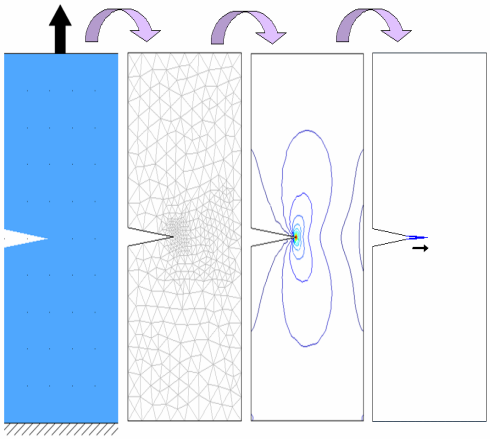

Figure 5.4: The percent error of the displacement in the final iteration.

5.3.1 The Cutoff Algorithm

The first analysis of the stick model was unsuccessful and no results were obtained. The root of the failure was traced to the force outputs from the initial analysis of the outer region. Recall the patch interface boundaries of this model were fully constrained in all directions. The artificially imposed constraints caused sever stress concentrations in the immediate vicinity of the corners that resulted in force anomalies well over 150% of the expected solution at the boundary extremities. Clipping these forces was necessary for the internal solver of the FEA to converge. The cutoff algorithm allowed the FEA to evaluate the patch region, and thus the overall coupled scheme could iterate.

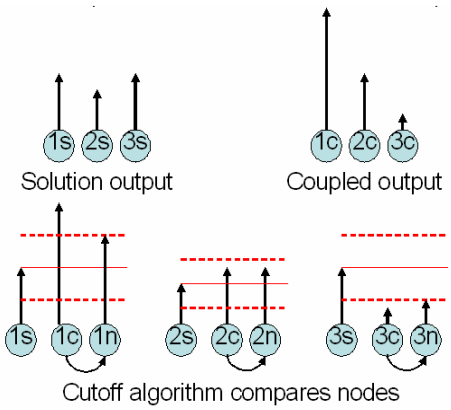

Figure 5.5: Visual representation of the cutoff algorithm.

The cutoff algorithm compared the solution force of each node along the patch boundary from a full FEA model of the stick (modeled with the same material properties and under the same loading conditions as the coupled analysis) to the corresponding node in the coupled analysis. If the force output of the node from the coupled analysis fell outside a specified range of the corresponding solution node the outlying force was clipped to the value it exceeded. If the force output from the coupled analysis fell within the specified range it retained its original value and was not changed. All solutions were checked to determine that the cutoff algorithm was not active on any node at convergence. This check implies a third convergence criterion. A visual rendition of the cutoff algorithm can be seen in

Figure 5.5. The cutoff range for the simulations presented in this paper was set to +/- 50% of the solution value. Validation of the cutoff algorithm can be found in Appendix A1-A2.

The horizontal lines visible at the boundary extremities in the first iteration (blue line), shown in Figure 5.6, are a result of the cutoff algorithm. The continuity of the final iterations (cyan line) shown in Figure 5.6 indicate they were unaffected by the cutoff algorithm. Analytical comparisons confirmed the final force and displacement results were within 50% of the solution and therefore unaffected by the cutoff algorithm.

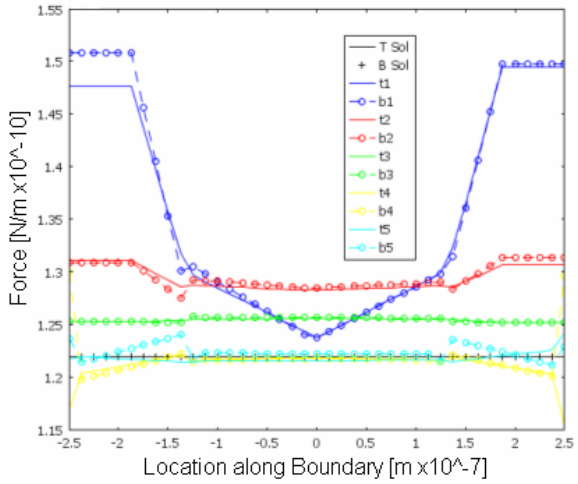

Figure 5.6: Effect of the cutoff algorithm on data near corners.

5.3.2 The Relaxation Algorithm

Without the relaxation algorithm the outputs of the coupled schemes oscillated about the expected solution as shown in Figure 5.7. The relaxation algorithm hastened the

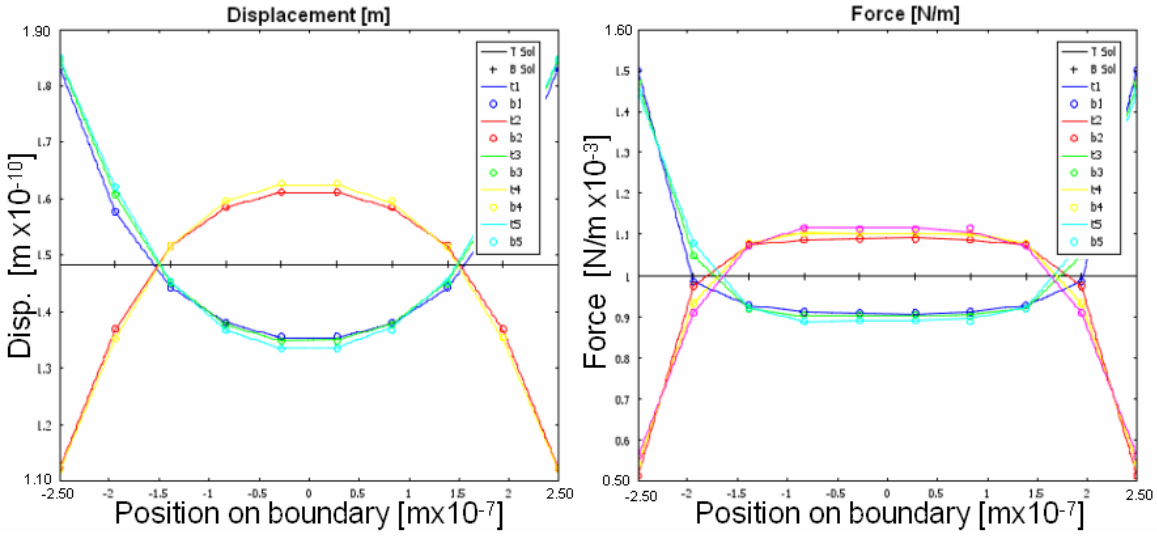

Figure 5.7: Effect of the cutoff algorithm during iterations: solution doesn't converge.

convergence of the system by dampening the oscillations. The relaxation algorithm compared the force outputs at each node from two consecutive iterations and determined a new force as a fixed percentage of the difference between the two force outputs. The relaxation algorithm is represented in pseudo-code with this set of equations:

$$F_f = F_o - \alpha\left(F_c - F_o\right) \qquad \textbf{(4)}$$

where $\boldsymbol{F_c}$ is the force from the current iteration, $\boldsymbol{F_o}$ is the force from the previous iteration, $\boldsymbol{\alpha}$ is the percentage the force is allowed to change, and $\boldsymbol{F_f}$ is the final force used in the subsequent iteration.

Validation of the Relaxation algorithm can be found in Appendix A3-A5. The relaxation algorithm was not applied during the first exchange of data as there was no previous data to compare too. For the simulations presented in this thesis the change in force between iteration was dampened to 50% ($\alpha = 0.5$). The value of 50% was selected because it allowed the models to converge to the tolerance specified in §4.1 within five iterations.

5.4 ENM-FEA: Uniform Load with Isotropic Properties

The success of the FEA-FEA scheme suggested the ENM-FEA scheme, with the same load and material settings would also prove viable. The ENM-FEA scheme was attempted and the convergence results as well as the percent error of the final iteration to the solution are presented in Figure 5.8 and Figure 5.9, respectively.

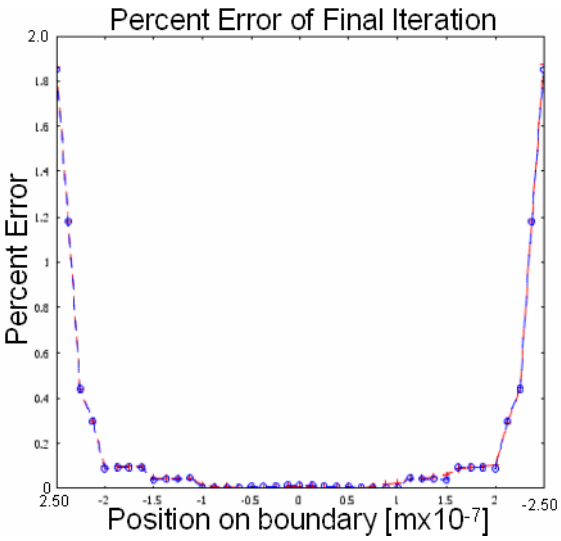

Figure 5.8: Percent error in force the final iteration for ENM-FEA simulation

The average accuracy of the final displacement values, with respect to the single-region FEA solution, was within 0.31%. The difference in output values between the last and second-to-last iteration was also within 0.41%. These convergence values were within the predefined limits of acceptability.

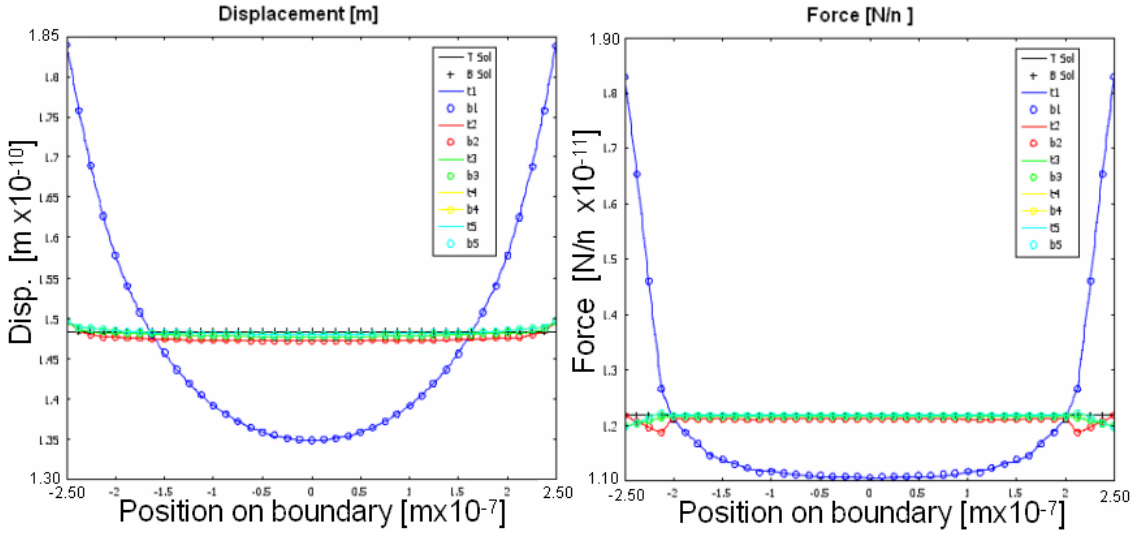

Figure 5.9: Simulation results for six iterations of a ENM-FEA coupled analysis.

5.4.1 Both Schemes: Non-Uniform Load with Isotropic Material Properties

The non-uniform but symmetric loading case (b) was then applied to the isotropic stick model and analyzed by both analysis schemes. The convergence and percent error graphs for each method are presented in Figure 5.10 and 5.11, respectively. In both cases the convergence of the last two iterations was within 0.47 % of each other and the overall accuracy of both models was within 0.39% of the expected solution value (~0.35% for FEA-FEA and ~0.39% for ENM-FEA).

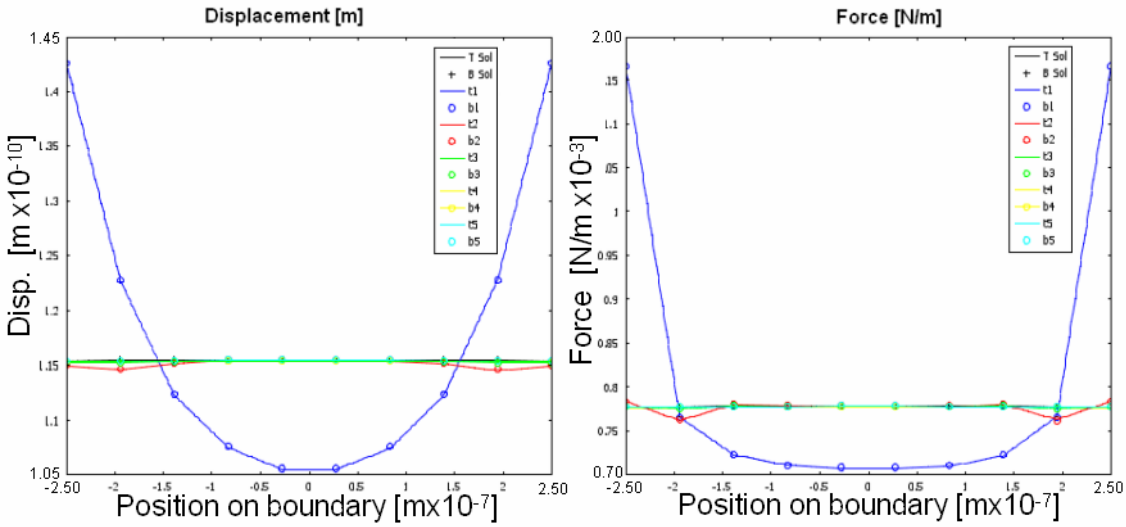

Figure 5.10: Convergence of FEA-FEA (top) and ENM-FEA (bottom) under loading case (b).

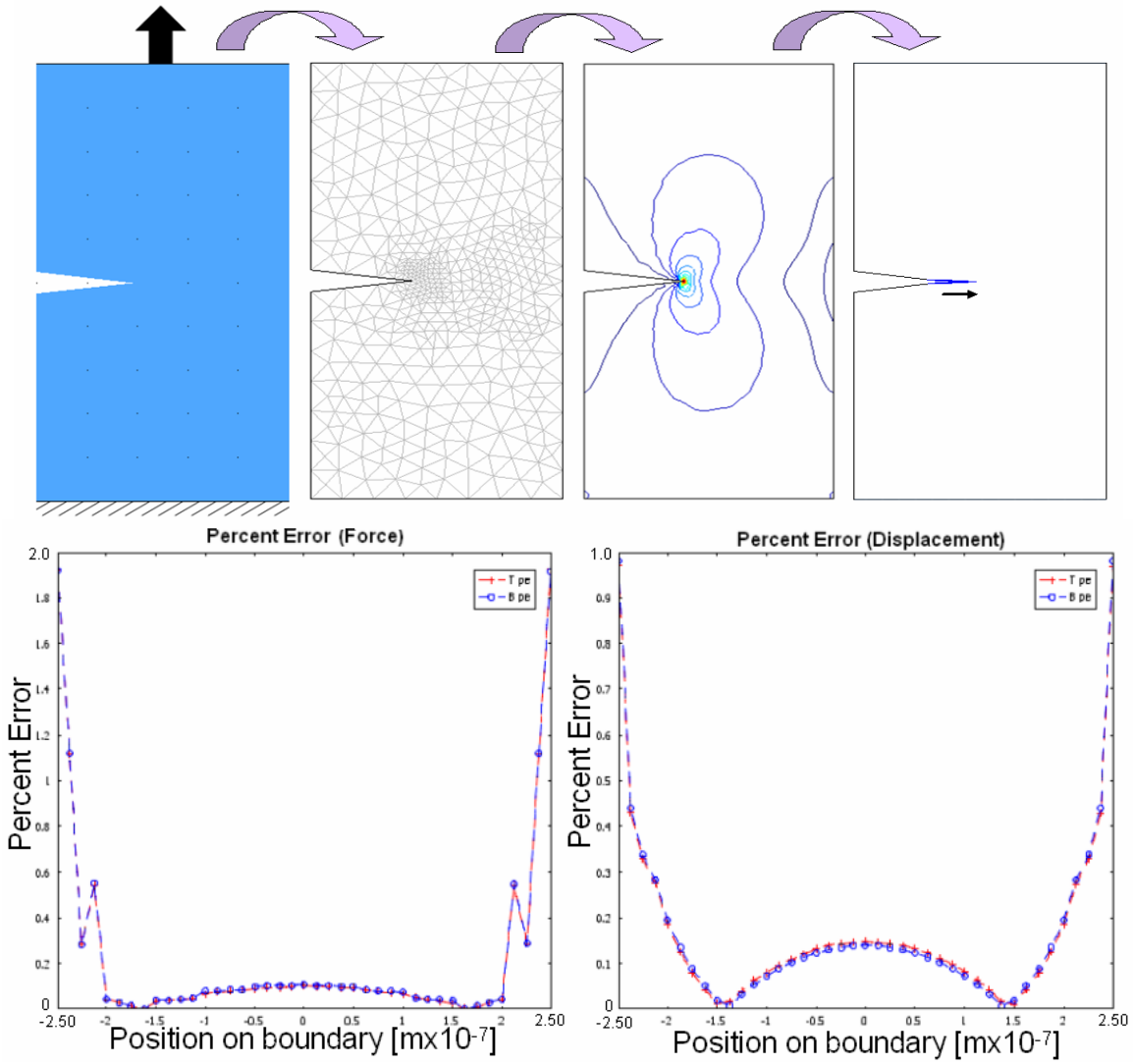

Figure 5.11: Percent Error of FEA-FEA (top) and ENM-FEA (bottom) under loading case (b).

The model was than subjected to a non-uniform non-symmetric load, case (c). The point constraints did cause mild perturbations in the stress field, as shown in Figure 5.12. However, these perturbations were sufficiently removed from the patch boundary to have

negligible effects on the forces at the patch boundaries. The convergence and accuracy of both schemes is shown in Figure 5.13 and 5.14, respectively. The average percent error with respect to the solution was ~1.8% and ~6.0% for the FEA-FEA and ENM-FEA simulation, respectively. The convergence fell within the acceptable limits, however the accuracy did not. In both cases the largest percent error occurred at the boundary extremities. The large percent error in the ENM-FEA model was caused by an interruption in the iterative process. The simulation was reattempted multiple times with no success. The cause of the problem was an internal error in the FEA software.

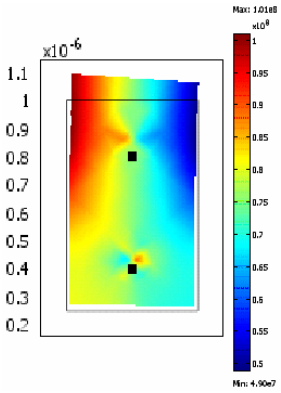

Figure 5.12: The effects of displacement constraints on the stress field in the upper portion of the stick model under loading case (c).

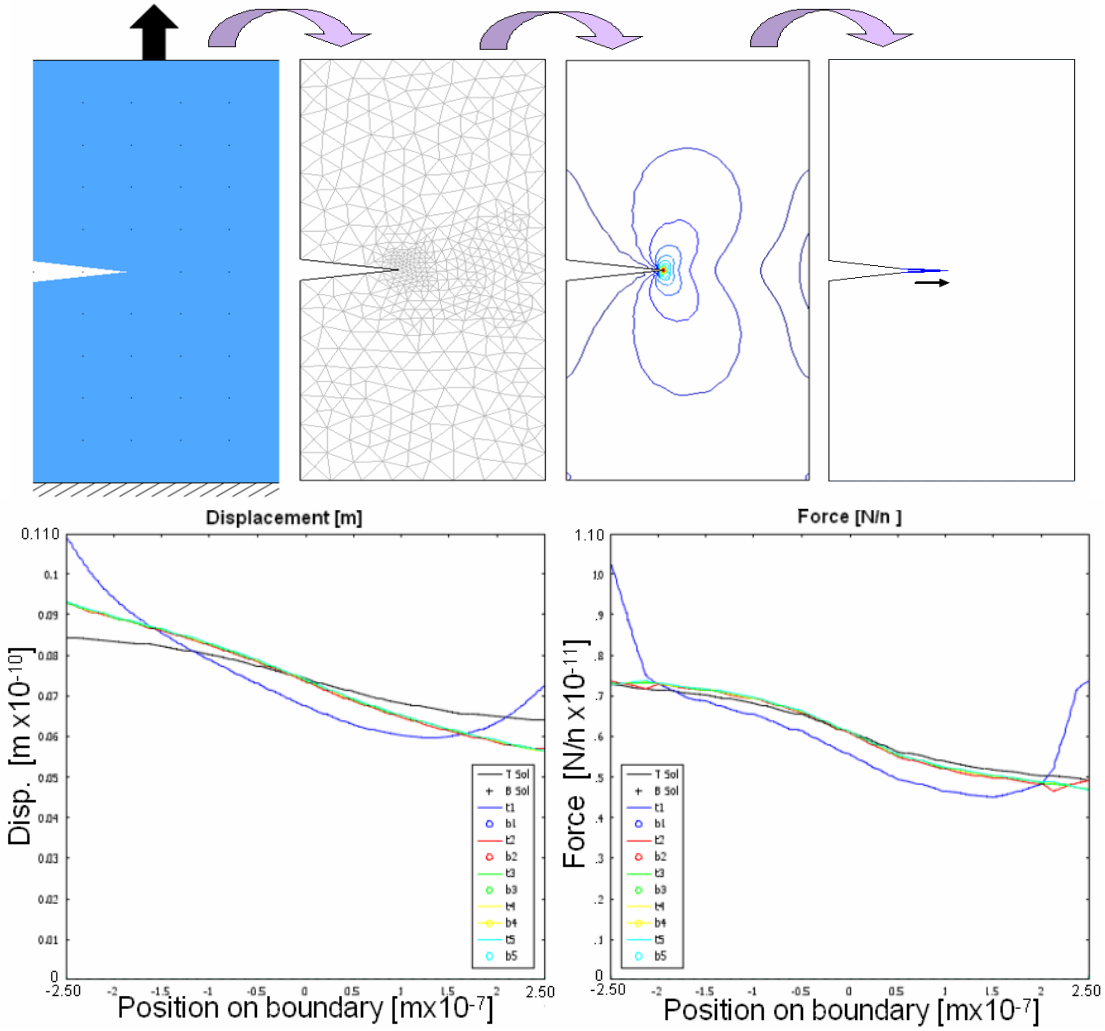

Figure 5.13: Convergence of FEA-FEA (top) and ENM-FEA (bottom) under loading case (c).

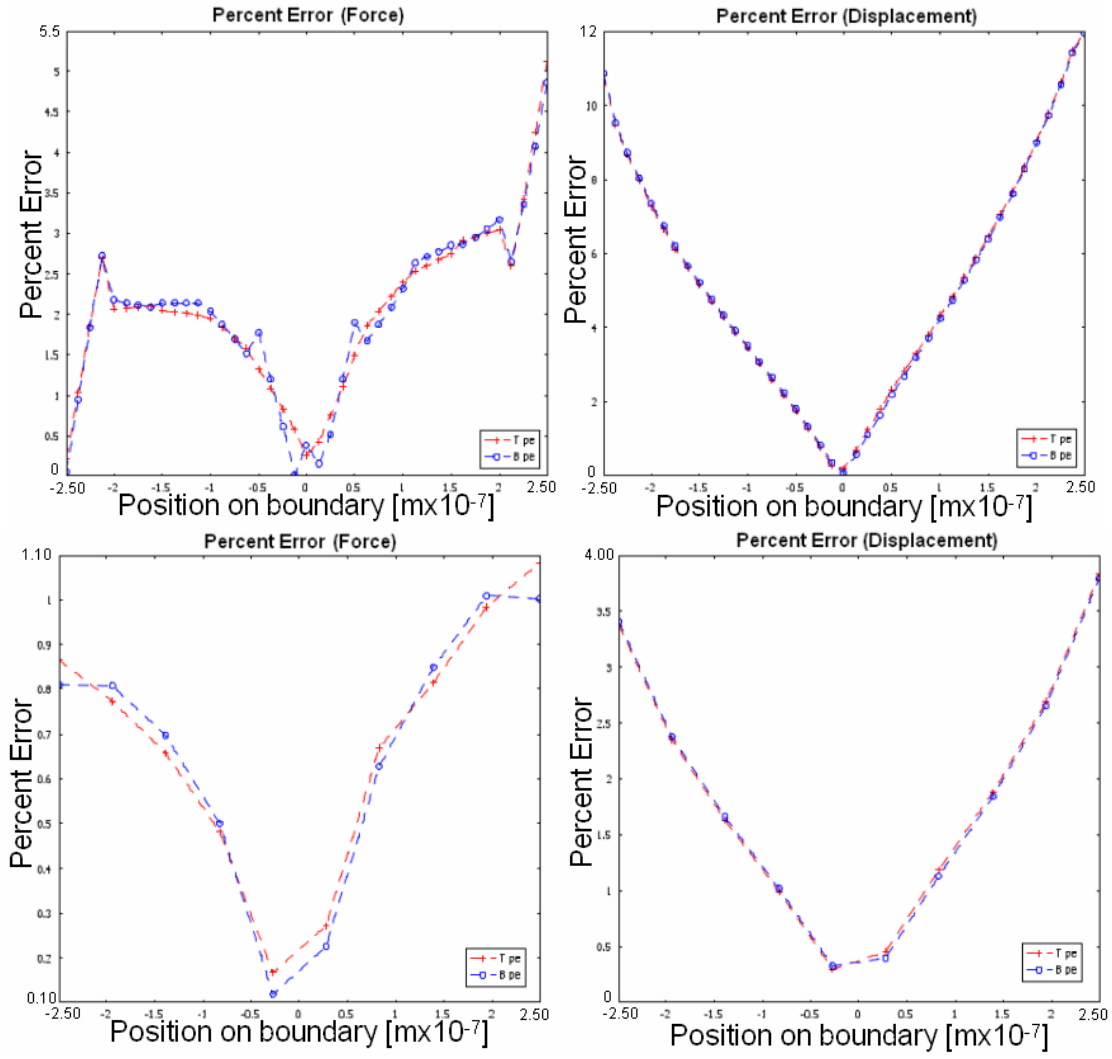

Figure 5.14: Percent Error of FEA-FEA (top) and ENM-FEA (bottom) under loading case (c).

5.4.2 Both Schemes: All loading Conditions – Anisotropic Properties

The stick model with anisotropic material properties was only subjected to loading cases (a) and (b). The results of case (a) for both FEA-FEA and ENM-FEA schemes are shown in Figure 5.15. In both instances the final iterations of the simulations converged to the within 0.27% of each other and the overall accuracy of the final iteration with respect to the solution was within 0.26%. Similar to the isotropic case, the

anisotropic ENM-FEA scheme did show a larger percent error in both force and displacement outputs at the boundary extremities.

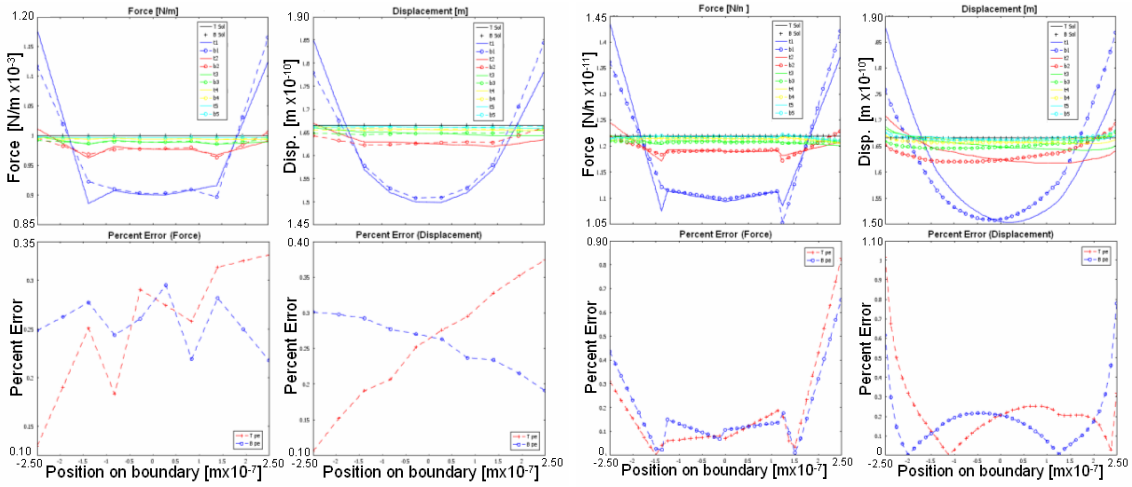

Figure 5.15: Convergence and Percent Error of FEA-FEA (left) and ENM-FEA (right) with anisotropic material properties under loading case (a).

The results of the convergence and accuracy of the FEA-FEA and ENM-FEA schemes under loading case (b) are presented in Figure 5.16. For both models the overall accuracy was within 0.52 % which was well within the acceptable limits. The non-uniform non-symmetric loading, case (c), was not applied to the anisotropic case as the accuracy of the isotropic models were not good and it was dubious that the results of the anisotropic model would be much better given the similar responses of the isotropic and anisotropic models under both loading cases (a) and (b).

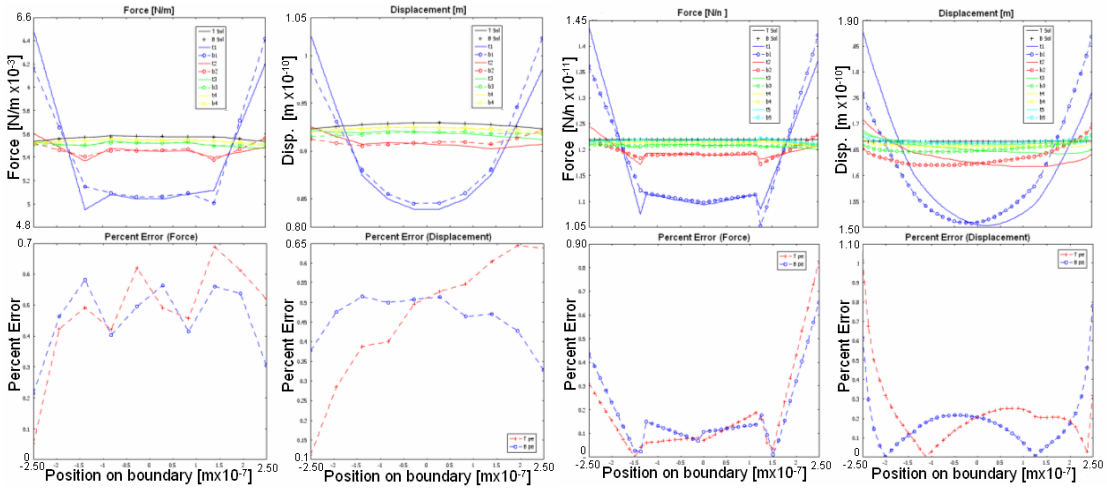

Figure 5.16: Convergence and Percent Error of FEA-FEA (left) and ENM-FEA (right) with anisotropic material properties under loading case (b).

5.5 Conclusions

The convergence and accuracy of the previous simulations indicate a strong likelihood that FEA-FEA and ENM-FEA schemes will be able to accurately model cracked geometries, with any material properties, as long as the data exchanged at the interface boundaries is symmetric. The accuracy of the non-uniform non-symmetric loading case was poor and the percent error was above the acceptable value. However, the convergence was well within in the acceptable limits. Convergence to an inaccurate value implies the iterative scheme works but there are errors in the data that is being input and output during the iterations. These errors are likely caused by the singularity in the geometry at the patch corners and the initial constraints.

The primary difference in accuracy between the ENM-FEA and FEA-FEA simulations occurred near the corners. This was expected for the same reasons described in §4.2 explaining the subtle discrepancy between the displacement outputs of the FEA and ENM analysis. In all cases the FEA-FEA results were more accurate than the FEA-ENM results because of the slight variation in material property characteristics explained

in §4.2. The ENM patch was shown to displace on average approximately 0.20% more than the FEA patch, under the same load. This inherent displacement discrepancy in addition to the corner affects, contribute to the decreased accuracy of the FEA-ENM simulations.

CHAPTER 6

ANALYSIS OF A FOUR-SIDED INTERFACE MODEL

6.1 Model Description

The four-sided interface model geometry was a 2000x1500nm rectangle with a 500x500nm patch in the center. As a result of the model's likeness to a block it will hereafter be referred to as the 'block' model. The overall dimensions, point constraints, and location of the external load application can be seen in Figure 6.1. Blue dots represent the location of points with zero y-displacement constraints, red dots indicate zero x displacement and displacement in all directions was fully confined at the green dot. The displacement constraints were all located on the axes of symmetry for both loading cases (a) and (b) and far enough from the patch boundaries to have any significant effect on the force outputs in loading case (c). The external loads were applied along the top and bottom boundary of the outer patch where the purple lines are in the Figure 6.1.

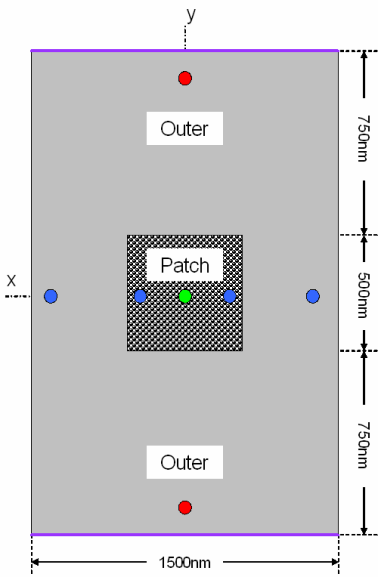

Figure 6.1: The block geometry.

6.2 Objective

The objective of the block geometry was to determine if the coupled analysis schemes could handle biaxial loading conditions. The convergence and accuracy of the models under the different loading conditions and with different material properties were recorded and studied to determine any shortcomings in the analysis schemes. A

comprehensive list of simulations involving the block geometry can be seen in Figure 6.2.

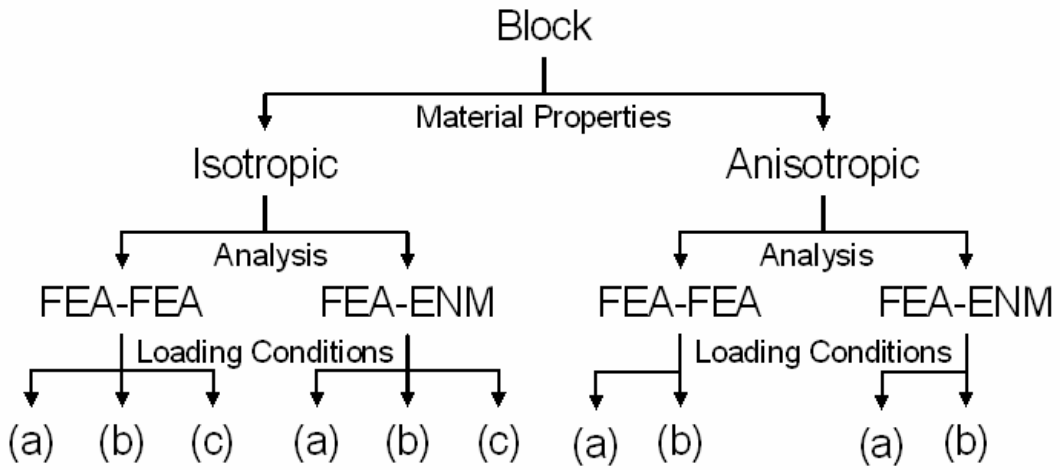

Figure 6.2: Modeling tree for the block geometry; (a), (b) and (c) refer to the loading cases shown in Figure 4.5 (10 total models).

The Figures presented in the following sections will show the convergence of the displacement along the horizontal and vertical boundaries of the patch. The solution values will be shown in black and the iterations will be denoted by the colors indicated by the legend in Figure 6.3. Since the loading is symmetric (in most cases) both the horizontal (top and bottom) and vertical (left and right) boundaries are shown on the same graph with the bottom and left values made negative. The 'T', 'B', 'L', and 'R' in Figure 6.3 refer to the top, bottom, left, and right boundaries, respectively. The absolute value of the percent error of each node in the last iteration with respect to the corresponding solution node will also be plotted.

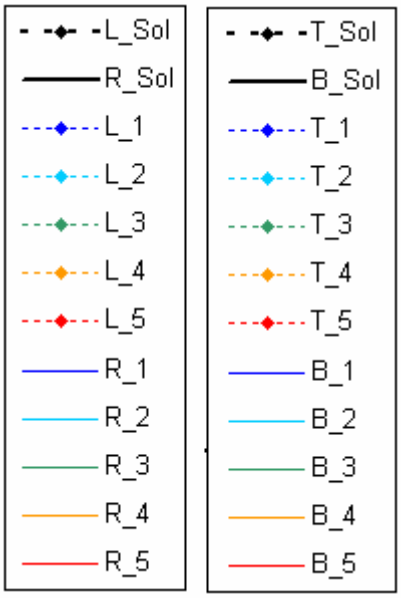

Figure 6.3: Legend for the subsequent convergence graphs.

6.3 Both Schemes: Uniaxial Loading with Isotropic Properties

The accuracy and convergence of the block model under loading case (a) were within 0.56% and 0.90%, respectively, for the FEA-FEA scheme and 1.90% and 0.80% for the ENM-FEA scheme. The convergence and accuracy results are shown in Figure 6.4 and 6.5 for the FEA-FEA and ENM-FEA schemes, respectively. The force outputs along the vertical boundaries were not shown, as they are extremely small and approximately zero (as expected). However, the results of the block model presented above required in addition (with respect to the cutoff and relaxation algorithm) data conditioning, which will be explained in the following paragraph.

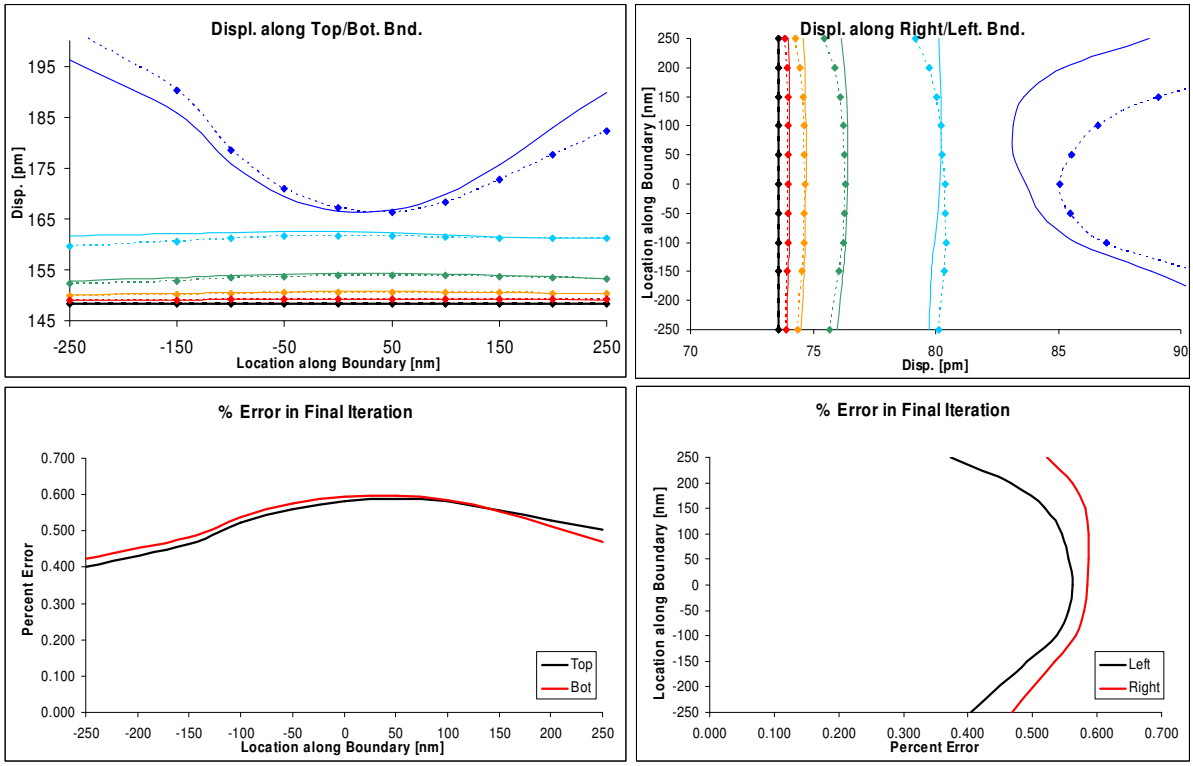

Figure 6.4: Convergence and Percent Error of FEA-FEA under loading case (a).

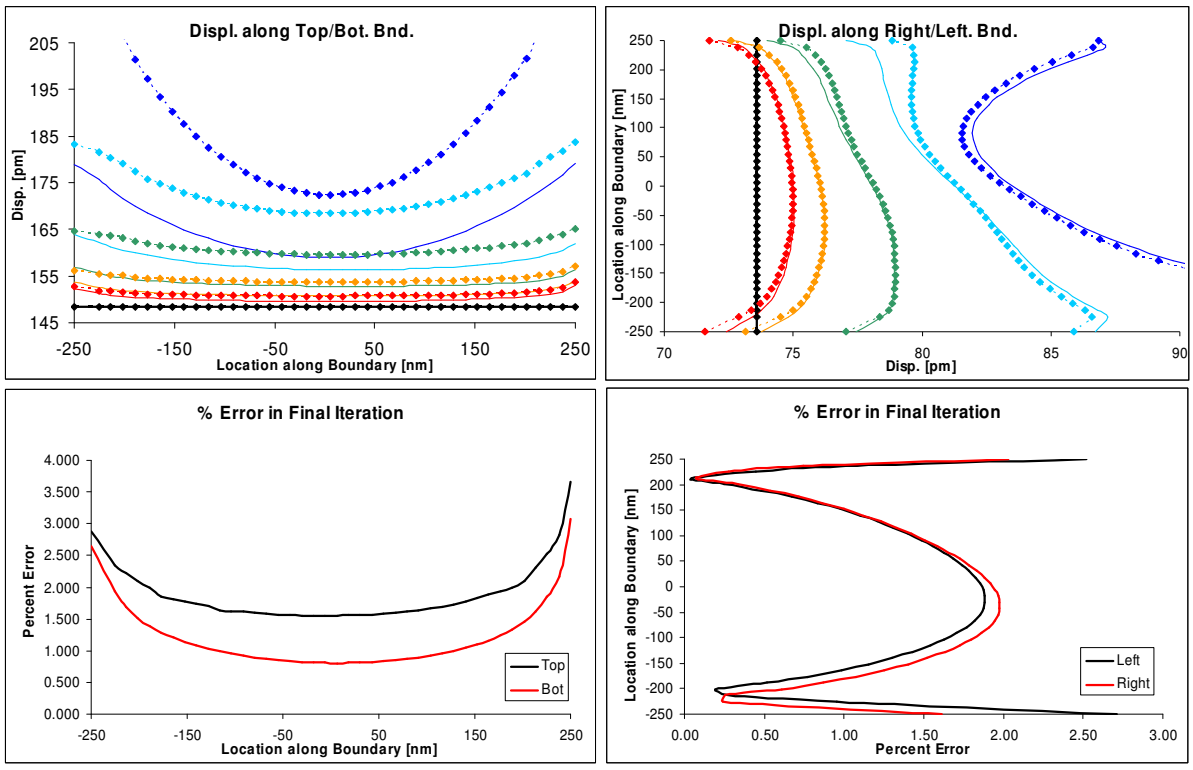

Figure 6.5: Convergence and Percent Error of ENM-FEA under loading case (a).

Preliminary analysis of the block geometry using the FEA-FEA scheme was inaccurate and the force outputs along the top and bottom boundary interfaces were non-symmetric about the x-axis. Closer examination of the top and bottom outputs showed the same drastic change in force at the bottom extremities as in the stick model. Unlike the stick model, these force anomalies persisted throughout the iterations but only in the bottom

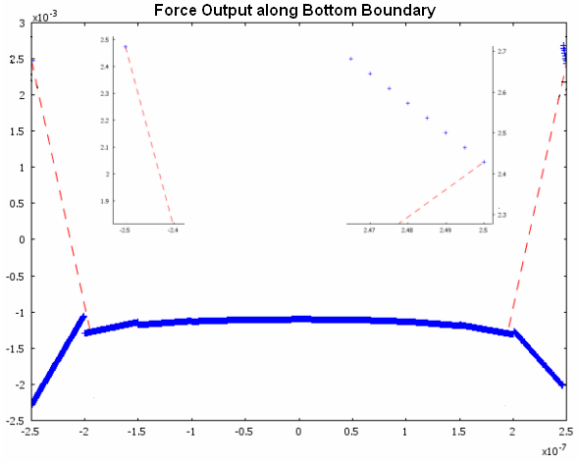

Figure 6.6: Force outputs from the bottom boundary of the patch every .05nm (blue) and 50nm (red).

boundary output. The bottom boundary output at the end of a simulation is shown in Figure 6.6 to highlight the stark change in force and its proximity to the singularities at the boundary corner. The cutoff algorithm prevented the corner forces from exceeding more than 50% of the solution value; however as the force along the remainder to the boundary converged the extremity forces remained at the cutoff limit.

To limit the effect of the corners on the overall accuracy of the model the force values at the boundary extremities were extrapolated from the force data collected between +/-2.0nm on the respective boundary. Implementing the extrapolation technique increased the accuracy of the models and resolved the lack of symmetry between the top and bottom force outputs. This methodology was applied to the simulations presented at the beginning of this section and for all subsequent block simulations. The correction was necessary to eliminate the near infinite force outputs predicted by FEA as the boundary approached a singularity at the corner and also to combat the less stiff corner nodes in the ENM described in §4.2.

6.4 Both Schemes: Non-Uniform Loading with Isotropic Properties

The results of both the FEA-FEA and ENM-FEA simulation of the block model under loading case (b) were acceptable. The accuracy and convergence were within 1.72% and 0.85%, respectively, for the FEA-FEA scheme and 1.62% and 0.76% for the ENM-FEA scheme. The convergence and accuracy results are shown in Figure 6.7 and 6.8 for the FEA-FEA and ENM-FEA schemes, respectively. As in previous simulation the majority of the error in the initial iterations occurred near the boundary corners.

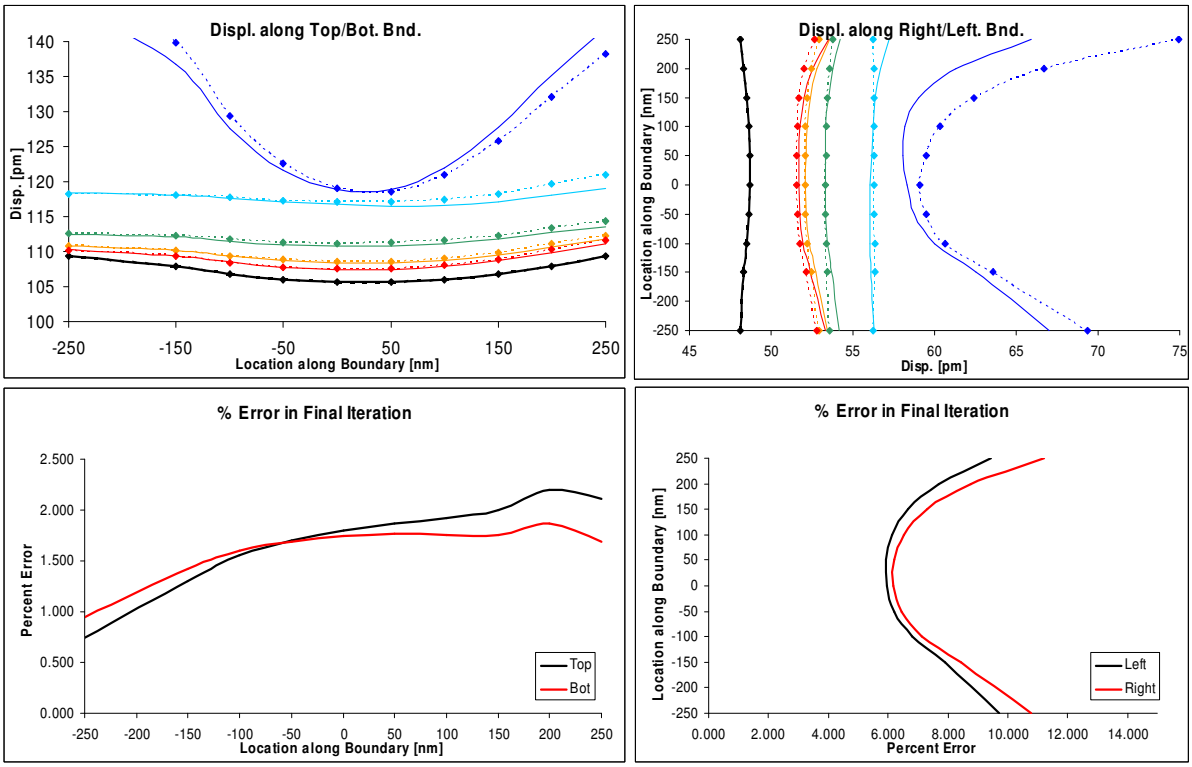

Figure 6.7: Convergence and Percent Error of FEA-FEA under loading case (b).

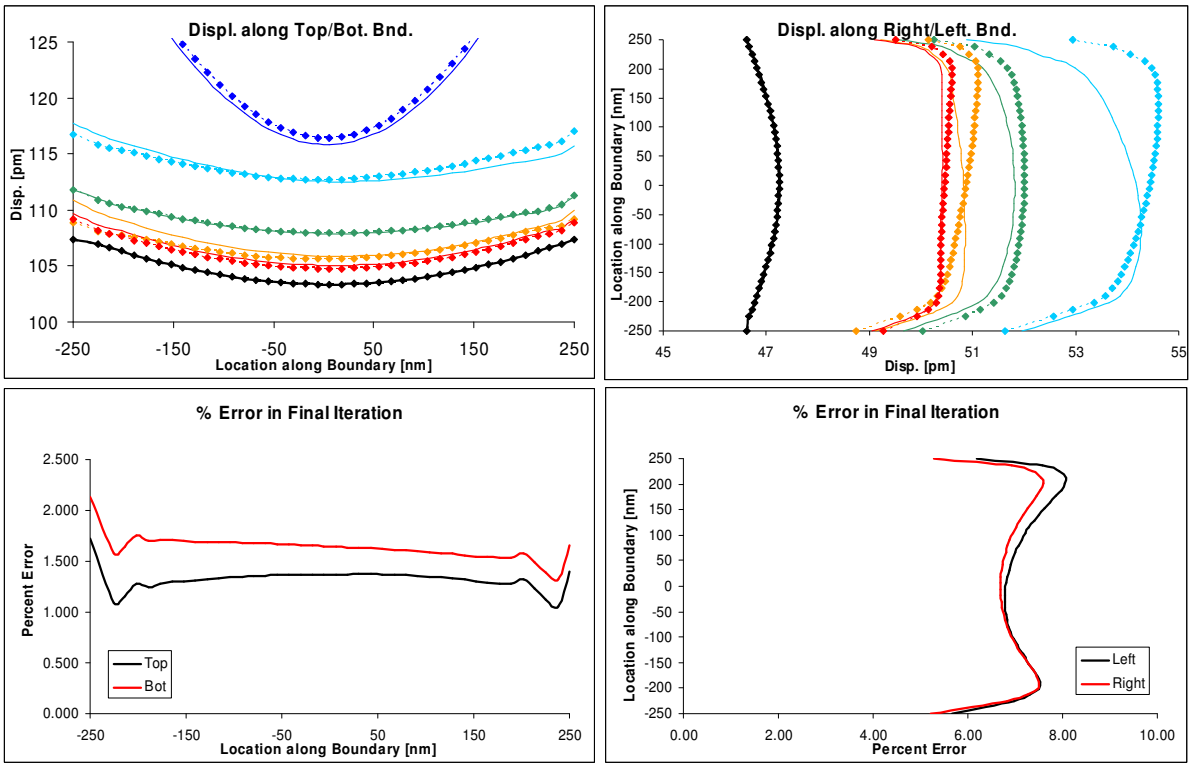

Figure 6.8: Convergence and Percent Error of ENM-FEA under loading case (b).

The accuracy and convergence of the block under loading case (c) were within 1.10% and 0.90%, respectively, for the FEA-FEA scheme and 1.50% and 2.0% for the ENM-FEA scheme. Therefore, both models were deemed acceptable under the previously defined criteria. The convergence and accuracy results are shown in Figure 6.9 and 6.10 for the FEA-FEA and ENM-FEA schemes, respectively.

Both schemes under loading case (b) and (c) converged well and with acceptable accuracy. The convergence of the force and displacements along the vertical interface boundaries was poor for both schemes under the non-uniform loading cases.

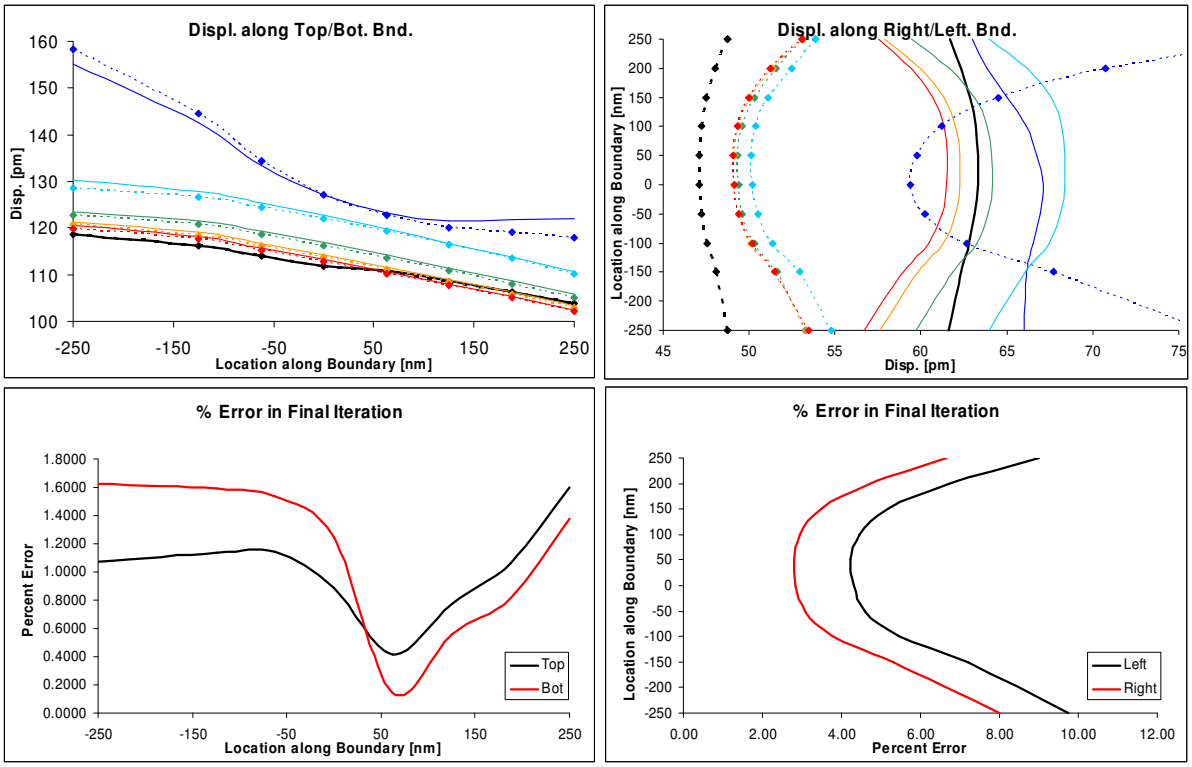

Figure 6.9: Convergence and Percent Error of FEA-FEA under loading case (c).

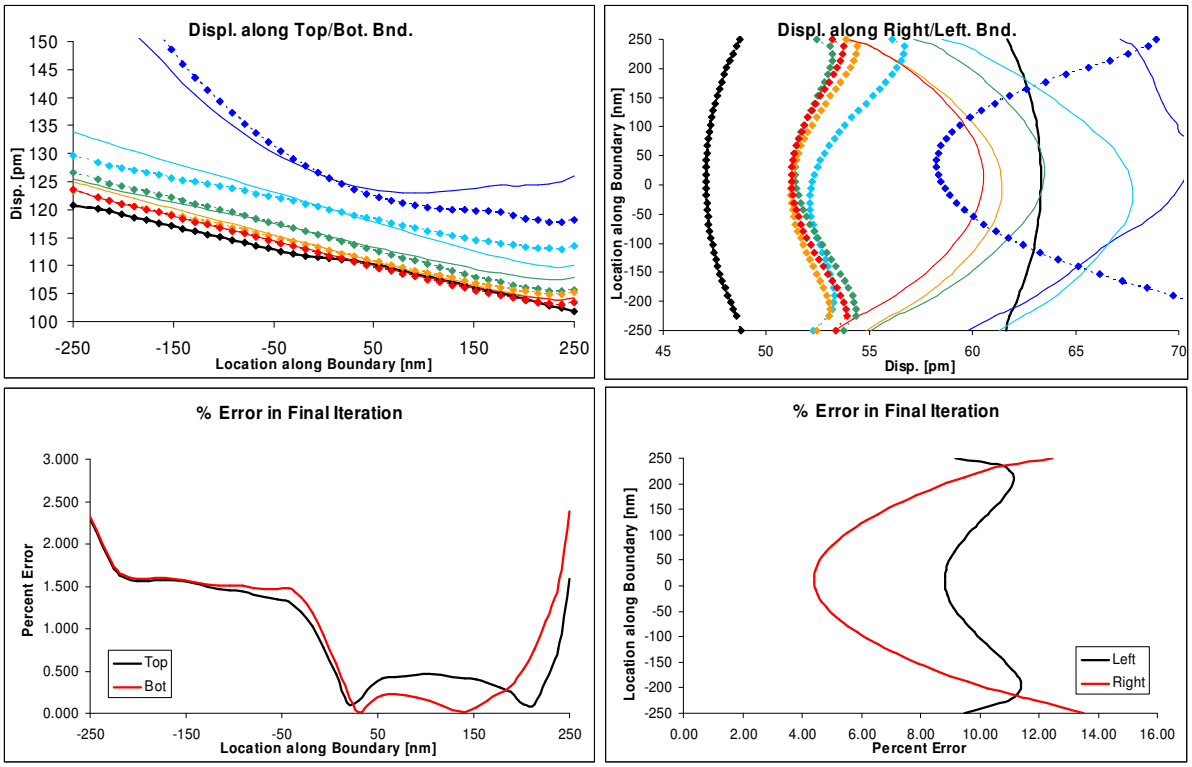

Figure 6.10: Convergence and Percent Error of ENM-FEA under loading case (c).

6.5 Both Schemes: All Loading Conditions with Anisotropic Properties

The accuracy and convergence of the anisotropic block under loading case (a) were within 0.50% and 0.80%, respectively, for the FEA-FEA scheme and 0.50% and 0.80% for the ENM-FEA scheme. Therefore both models were deemed acceptable. The convergence and accuracy results are shown in Figure 6.11 for the FEA-FEA and ENM-FEA schemes.

The results of both the FEA-FEA and ENM-FEA simulation of the block model under loading case (b) were also acceptable. The accuracy and convergence were within 1.85% and 0.80%, respectively, for the FEA-FEA scheme and 1.85% and 0.80% for the ENM-FEA scheme. The convergence and accuracy results are shown in Figure 6.12 for the FEA-FEA and ENM-FEA schemes.

The results of both the FEA-FEA and ENM-FEA simulation of the block model under loading case (c) were also acceptable. The accuracy and convergence were within 0.55% and 0.80%, respectively, for the FEA-FEA scheme and 1.90% and 1.29% for the ENM-FEA scheme. The convergence and accuracy results are shown in Figure 6.13 for the FEA-FEA and ENM-FEA schemes.

The accuracy of the forces and displacement values exchanged across the vertical patch boundaries was poor. However, the convergence was acceptable. This phenomenon was also observed in the isotropic block simulation and is addressed in the Conclusions section of this chapter.

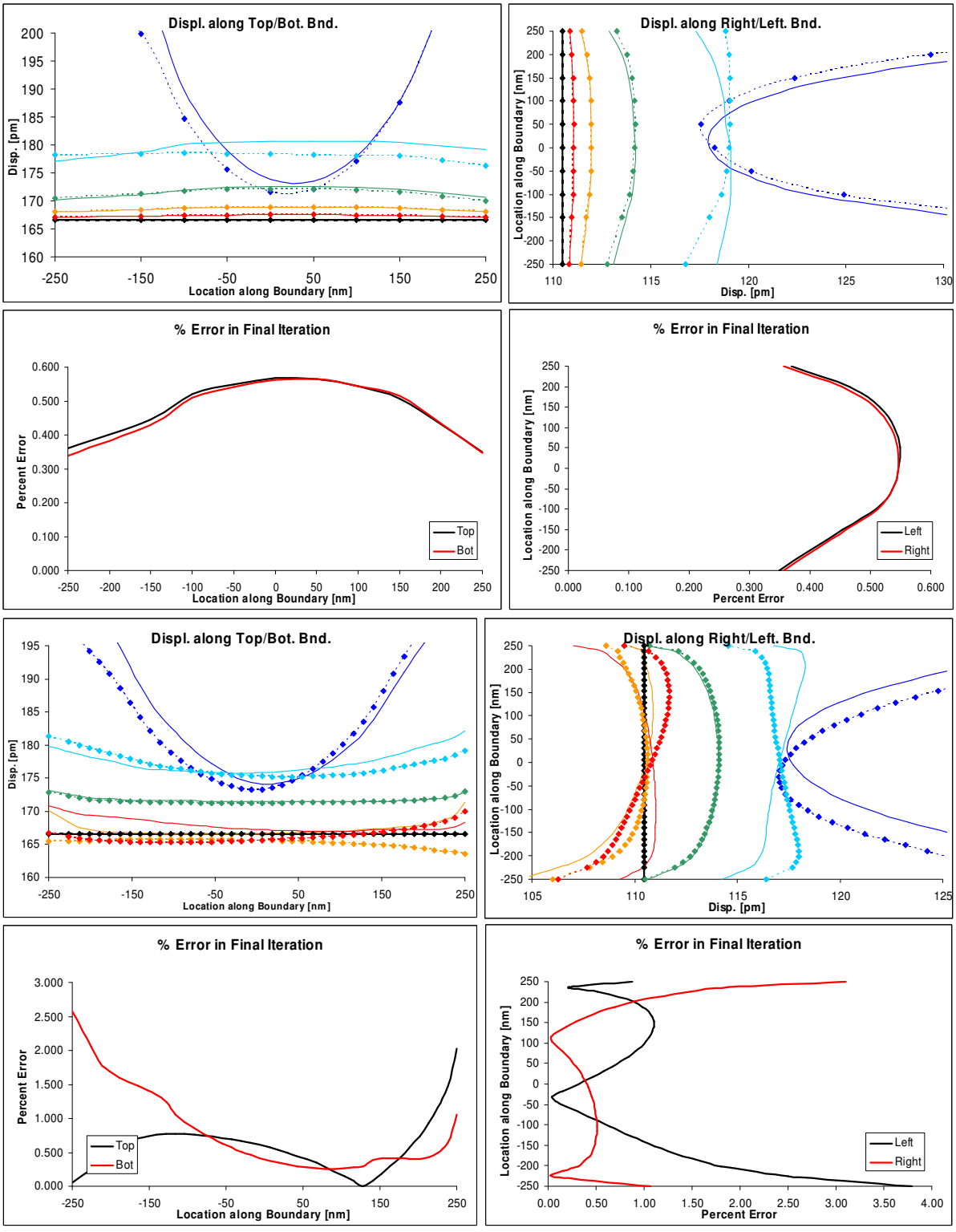

Figure 6.11: Convergence and Percent Error of FEA-FEA (top) and ENM-FEA (bottom) with anisotropic material properties under loading case (a).

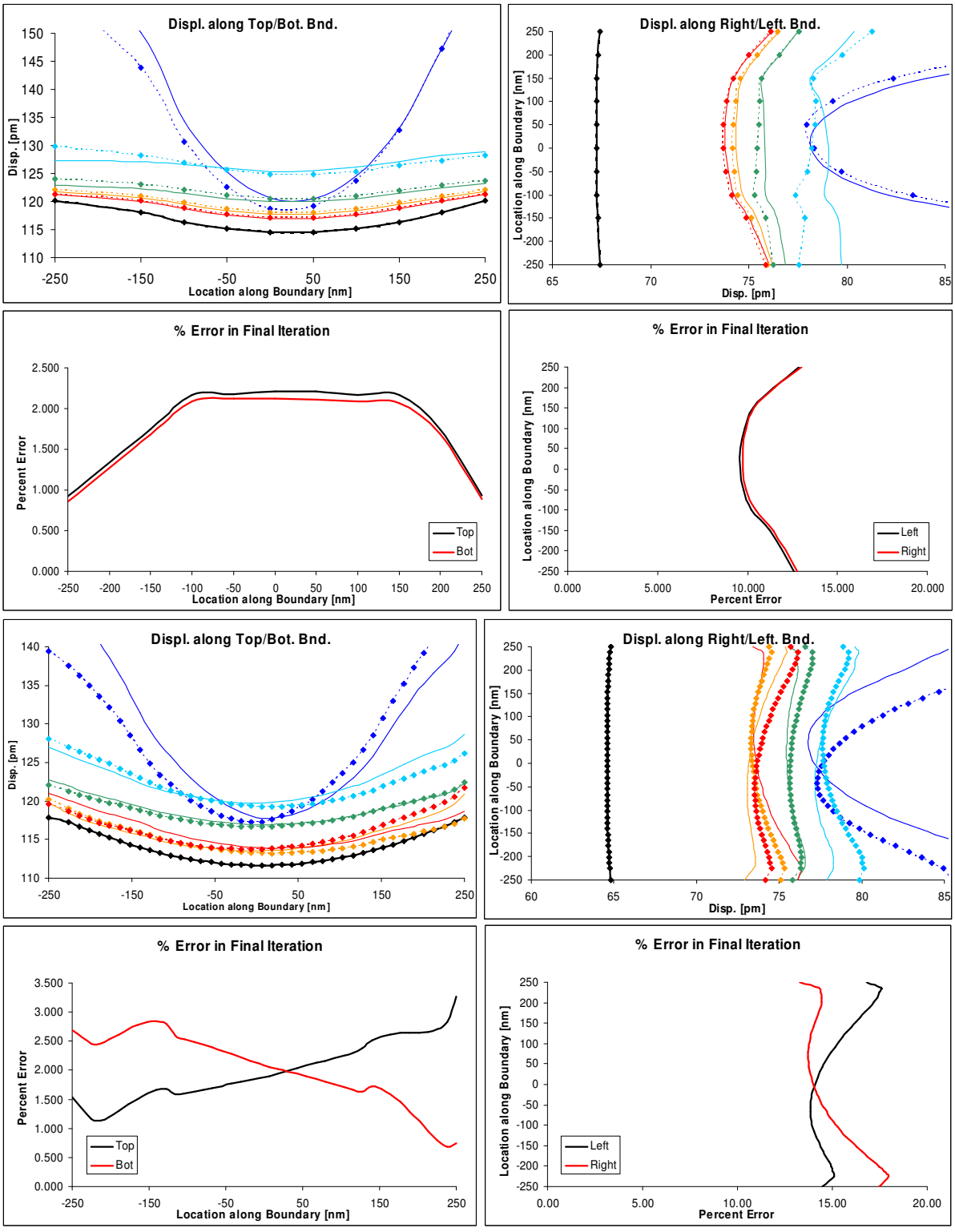

Figure 6.12: Convergence and Percent Error of FEA-FEA (top) and ENM-FEA (bottom) with anisotropic material properties under loading case (b).

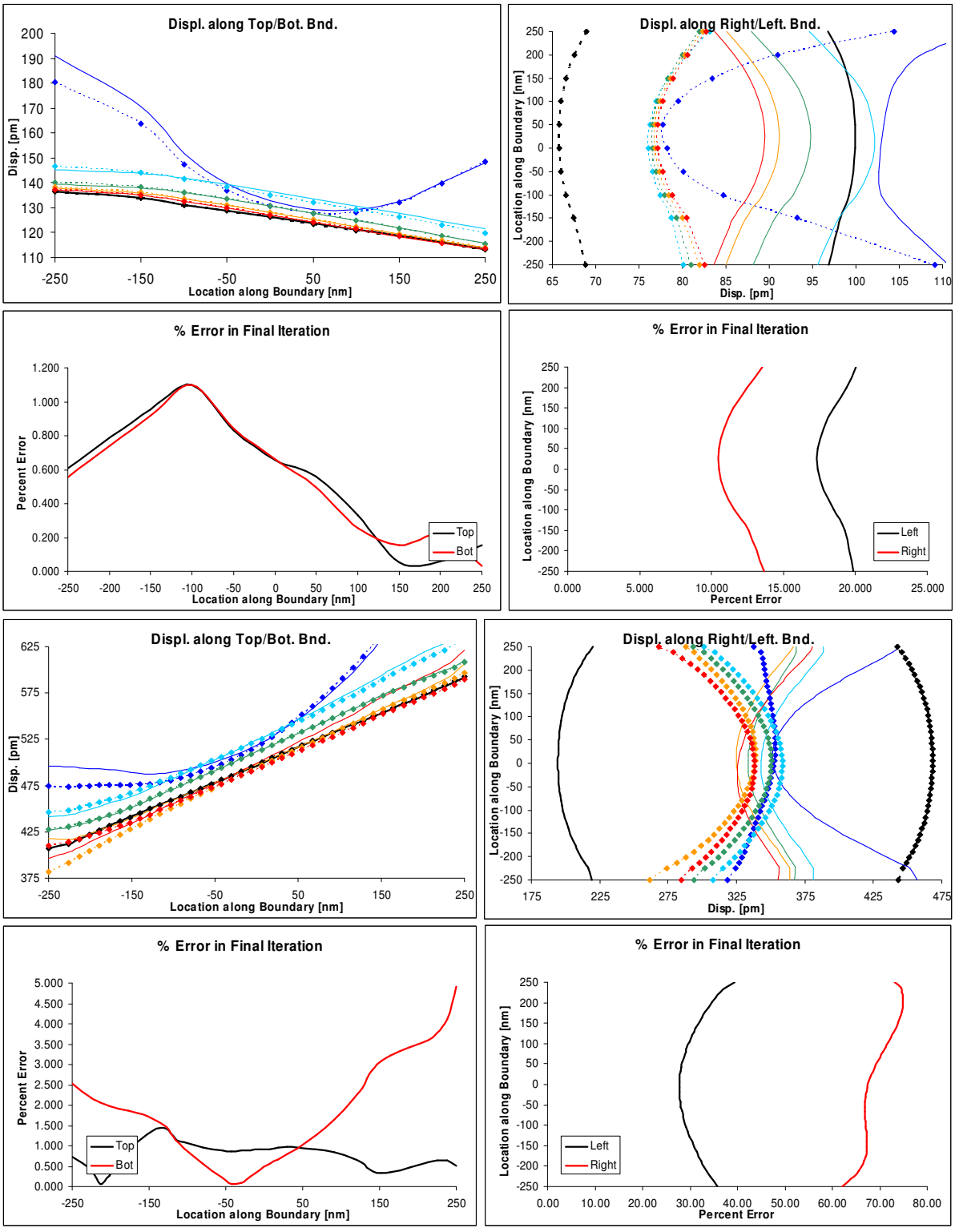

Figure 6.13: Convergence and Percent Error of FEA-FEA (top) and ENM-FEA (bottom) with anisotropic material properties under loading case (c).

6.6 Conclusions

The accuracy and convergence of the coupled analysis schemes was within the range of acceptability, as defined in §4.1 for all the loading case. Extrapolating the boundary data near the corners has proven to effectively mitigate the corner effects that hindered preliminary models. The increased material surrounding the corner also played a role in constraining the displacement of the corner node.

The response of the block models under loading case (c) was more accurate than the response of the stick model under the same loading. This is most likely a result of the aforementioned additional data conditioning and constraints present in the block model, as the majority of the error in the stick model occurred at the boundary extremities. Applying a similar data extrapolation algorithm to the stick model could have increased the accuracy of the simulations.

The similarity in results between both isotropic and anisotropic simulations further confirms the assertion that the coupled modeling schemes are independent of material properties.

The convergence of the displacement values along the vertical interface boundaries is acceptable for all loading cases; however its accuracy is poor. This is likely a consequence of the horizontal forces being derived from the contraction of the model rather than from an applied external force. The majority of the displacement along the vertical boundaries results from the perpendicularly applied force along the top boundary (which is increasingly less accurate as it approaches the corner). The force anomalies coupled with the decreased horizontal stiffness of the boundaries surely contribute to the inaccuracies as well. Overall the magnitude of the difference in horizontal displacement

in the patch is small compared to the vertical displacements along the top and bottom boundaries.

CHAPTER 7

ANALYSIS OF MODELS CONTAINING CRACKS

Four different alterations were made to the two and four-sided transverse interface models discussed in the previous sections in order to mimic crack conditions. In all cases the external loading along the outer portion of the model was uniform, case (a), and the rigid body constraints were kept intact whenever possible. The models with cracks were analyzed by both FEA-FEA and ENM-FEA schemes. Due to the similarity in results between the isotropic and anisotropic cases established in prior simulations it was deemed unnecessary to run simulations with both sets of material properties – success with one set of material properties would indicate a high likelihood of success with any material properties. The isotropic material properties were selected for use in the simulations as a matter of convenience.

7.1 External (relative to patch) Cracks

External cracks refer to cracks located outside the patch. Two external crack scenarios were modeled. In the first case there was only one external crack, and in the second case there were two. A zero force input was applied to the nodes in the ENM representing the crack tip. The complete listing of the external crack scenarios modeled can be seen in Figure 7.1. Further information, results, and conclusions for the models will be presented in the following sections.

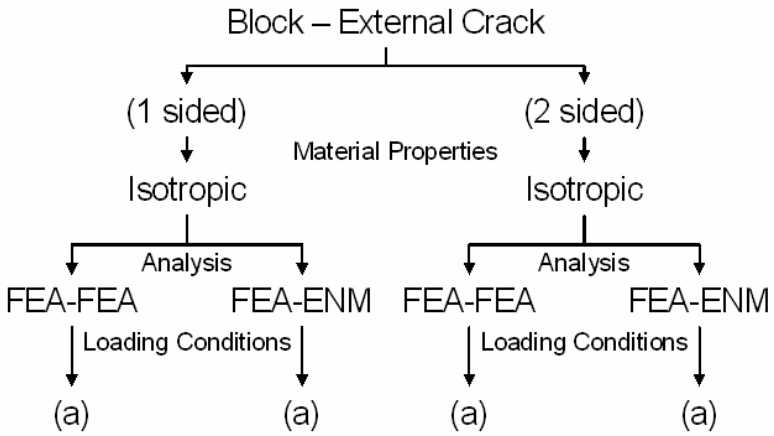

Figure 7.1: Modeling tree of models with cracks in geometry (4 total models).

7.1.1 One Sided External Crack – Geometry and Objective

The first scenario involved removing a section of material from the outer potion on one side of the block geometry, as shown in Figure 7.2. The height of the crack was a constant 100nm so the corners at its tip would conveniently align with nodes along the patch boundary. The alteration to the geometry would result in a non-uniform non-symmetric loading condition, similar to that induced by loading case (c). Therefore, the model was expected to have similar accuracy and convergence characteristics as the isotropic block model under loading case (c).

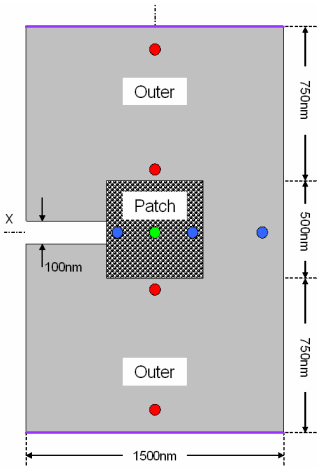

Figure 7.2: Block geometry with one external crack.

7.1.1.1 Results and Conclusions

The results of the one-sided crack simulation for both the FEA-FEA and ENM-FEA schemes are presented in Figure 7.3. The convergence of both the FEA-FEA and ENM-FEA schemes was acceptable at 0.63% and 0.26%, respectively. The accuracy of

the models was approximately 9.0% and 9.25% for the FEA-FEA and ENM-FEA schemes. These values were not acceptable. The majority of the error along the top and

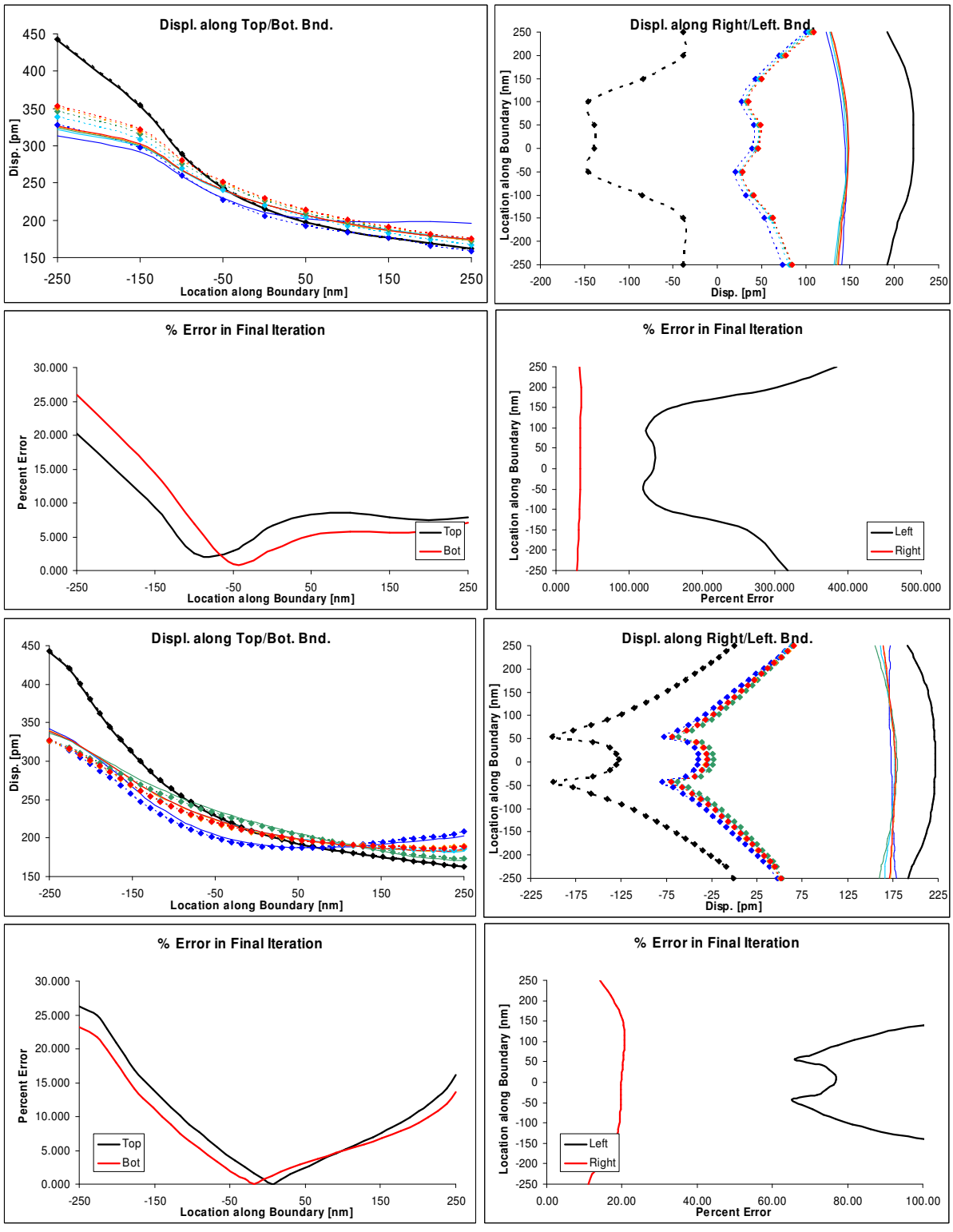

Figure 7.3: Convergence and Percent Error for FEA-FEA (top) and ENM-FEA (bottom) under loading case (a) with one external crack in geometry.

bottom boundaries occurred near the boundary extremities, especially near the crack side corner where the error in displacement reached its maximum at approximately 20% and 16% for the FEA-FEA and ENM-FEA schemes, respectively.

The horizontal displacement along the vertical boundaries followed the same trends predicted by the solution value however the accuracy averaged a 18% error on the non-cracked side and nearly 80% error on the cracked the side. This was not surprising considering the high error along the vertical boundaries previous observed in the block model simulations in combination with the addition of the two singularities present at the crack tip. The horizontal displacement solution value, derived from the single-region FEA model, is also suspect as the forces and subsequently the displacements of the singe-region FEA model would increase to infinity as they approached the singularities at the corner. Therefore, the 'solution' value itself might not be accurate rendering the percent error near the crack tip irrelevant.

7.1.2 Two Sided External Crack – Geometry and Objective

This next case was very similar to the previous case, but with material removed from the outer region at either side of the patch, as shown in Figure 7.4, to mimic two cracks. The crack height was the same as in the previous model. It was hoped that by locating two cracks symmetrically about the patch the resulting stress along the boundary would be symmetrical and similar to loading case (b) applied to the un-cracked

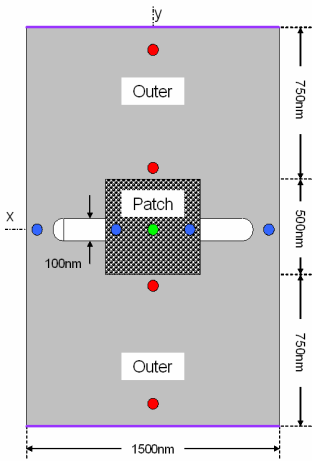

Figure 7.4: Block geometry with two external cracks.

models.

7.1.2.1 Results and Conclusions

The results for the two sided crack simulation are shown in Figure 7.5 for both the FEA-FEA and ENM-FEA analysis schemes. The accuracy and convergence of the FEA-FEA model was with 7.4% and 0.20%, respectively. The convergence of the FEA-ENM model was 0.23% and its accuracy was 9.0%. Both models are considered to be inaccurate based on the criteria defined in §4.1. The overall concavity of the simulation results is opposite to that of the solution and the average error is only small because the solution curves overlap. The standard deviation is two orders of magnitude larger that that of the un-cracked block geometry under loading case (c). Although inaccurate with respect to the solution, the results of the two-coupled schemes are in relative close agreement with each other. Since both schemes had been proven to accurately converge under simple loading case it can be concluded that the error is a result of the input and output data rather than the schemes.

The convergence graphs of the force outputs further highlight the effect of the corners on the boundary outputs. Similar to the one sided crack simulation the force output along the top and bottom boundaries go awry at the corners failing to capture the true force trend. The accuracy of the horizontal displacements along the vertical boundaries was better than observed in most of the other simulations. This can be attributed to the increased forces that were present given the geometry and loading of the model in this scenario. Form these results it can be surmised that increasing the horizontal force in the model will increase the accuracy of its horizontal displacements.

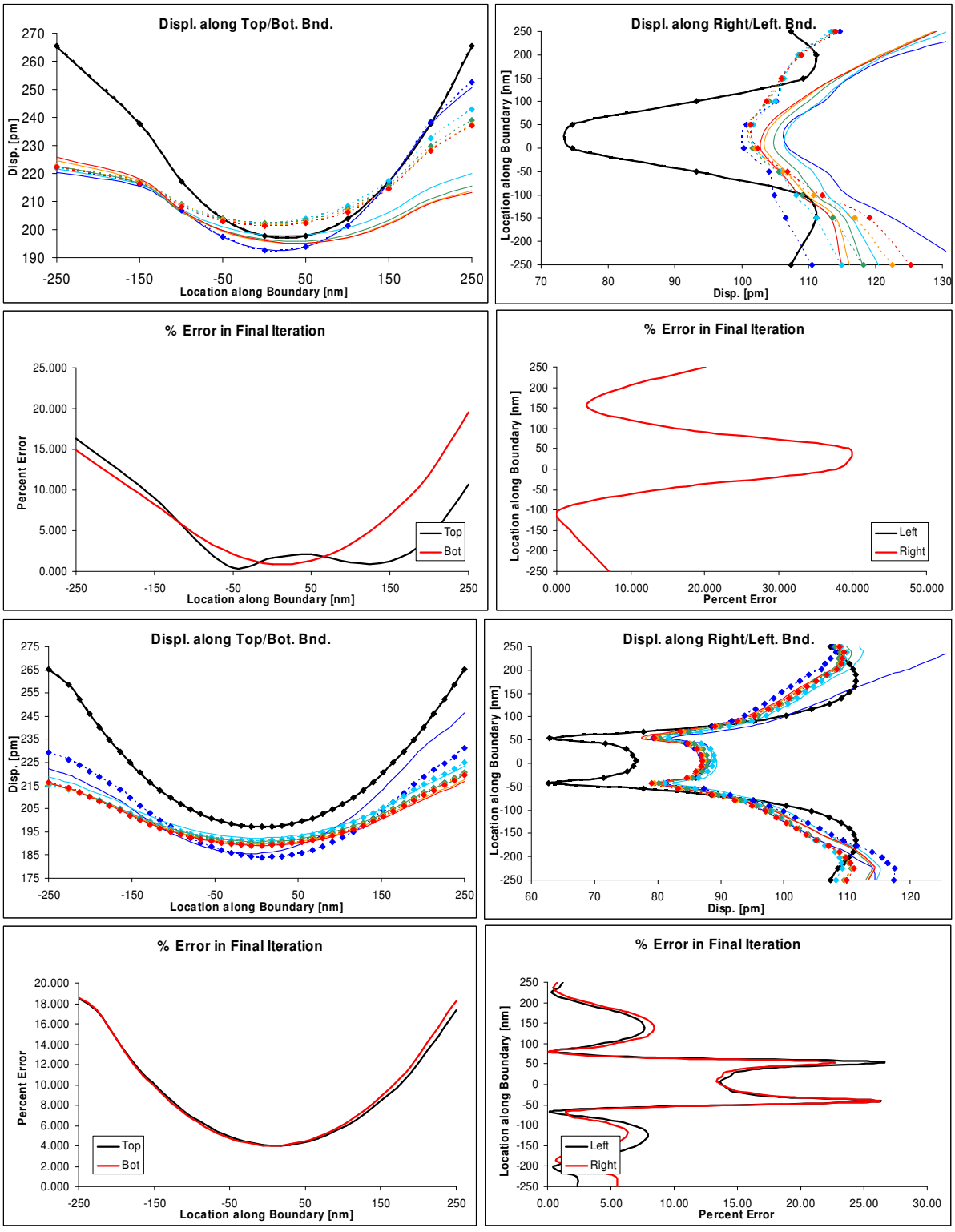

Figure 7.5: Convergence and Percent Error for FEA-FEA (top) and ENM-FEA (bottom) under loading case (a) with two external cracks in geometry.

7.2 Internal (relative to patch) Cracks

Internal cracks were represented by geometric vacancies in the model within the patch. In the case of the ENM the horizontal and vertical springs attaching the nodes in the area representing the crack were eliminated by setting their value to zero. The diagonal spring constants were set to 0.001, which is essentially zero however a numerical value was necessary for the solving the ENM.

7.2.1 Stick: Geometries and Objective

The objective of the internal crack models was to explore how the models would converge under a uniform external load with a small symmetric flaw in the patch geometry. The size of the crack was varied to determine if there was any relation between crack size and either the convergence or accuracy of the model. Success of these models would indicate that modeling parts with small cracks or flaws at the nano-level with a coupled ENM-FEA analysis scheme was possible.

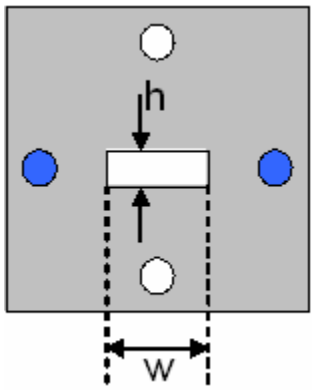

Figure 7.6: Patch with an internal crack.

Both of the internal cracks modeled were centered along the horizontal line of symmetry in the patch region. The first crack was 25x100nm and analyzed with both the FEA-FEA and ENM-FEA schemes; the second was 10x70nm and modeled only with the FEA-FEA scheme. The later was modeled with only the FEA-FEA scheme to study the effect of crack size on the solution accuracy and convergence. Additional point constraints (in the x-direction) were added to the FEA patch model and are shown in Figure7.6 as the white dots. Although the crack size is below the resolution of the FEA,

the error incurred by its existence will have subsided before reaching the patch boundaries and should have minimal effect on the output data.

The smaller crack could have been modeled with the FEA-ENM scheme but would require additional refinement of the elastic network in the vicinity of the crack. The location of the crack also eliminated the only x displacement constraint in the patch model, resulting in a model that could succumb to rigid body. However, since there were no external loads in the x direction applied to the patch in the stick model and the loading along the top and bottom boundaries is symmetric (and remains approximately symmetric throughout the simulation), the patch region is stable and the lack of constraint in the x direction is negligible.

7.2.1.1 Results and Conclusions

The convergence and percent error graphs for the FEA-FEA simulation of the model containing a 10x70nm crack are presented in Figure7.7. The accuracy and convergence of the model was acceptable, and slightly better than for the FEA-FEA model with the larger crack, at 0.62% and 0.80% respectively.

The displacement results

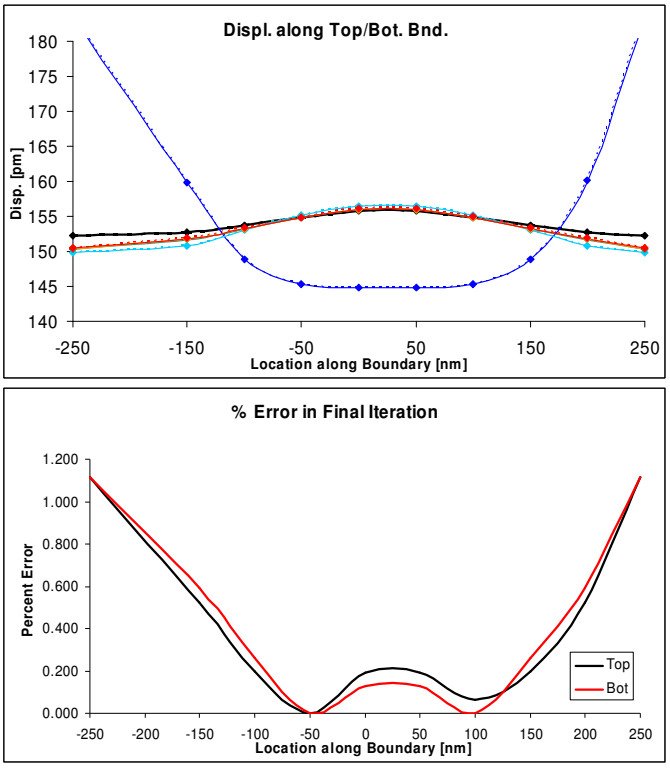

Figure 7.7: Convergence and Percent error of FEA-FEA for stick model with internal crack (10x70nm).

for the geometry containing the larger, 25x100nm, crack size along the top and bottom boundaries of both the FEA-FEA and ENM-FEA schemes demonstrated accurate convergence to the solution values. The accuracy of the FEA-FEA and ENM-FEA schemes was acceptable at 1.30% and 1.42%, respectively. The convergence of both the FEA-FEA and ENM-FEA schemes was also acceptable at 0.90% and 0.84%, respectively.

The simulation results for all the internal crack scenarios in the stick geometry were accurate and very similar to the results of the initial stick model with no internal cracks present under loading case (a). This observation is expected due to the minimal effect of the internal crack on the force at the boundary resulting in a nearly uniform loading distribution at equilibrium.

The slightly better accuracy of the model with the smaller crack size indicates that the convergence of the model could be dependent on the magnitude of the force along the boundary, although the difference in accuracy falls within the range of error. Further studies will need to be conducted to confirm this.

7.2.2 Block: Geometries and Objectives

The block model with an internal crack was only analyzed using the FEA-FEA scheme. An analysis with the ENM-FEA scheme was attempted however, with externally applied forces in the x direction and no x constraint in the patch the model was unstable and large rigid body motion occurred during the simulation.

The outer region of the model was the same as described in Section 6.1. The patch region was exposed to the same two internal crack sizes and constrained in the same manner as the patch for the stick model discussed in the previous section.

The objective of this model was to see if the analysis schemes could handle simulations involving the biaxial loading of a patch region containing a crack. Also, the size of the internal cracks was much smaller than the external cracks and consequently caused smaller perturbations in the forces along the boundary.

7.2.2.1 Results and Conclusions

The results for both crack geometries demonstrate accurate convergence and are shown in Figure 7.8. The smaller internal crack size resulted in a slightly more accurate solution (0.62% compared 1.30%) than that of the larger crack, however both values fell within the same margin of error. The convergence of the simulations was also acceptable for both cases at 0.80% and 0.90% for the smaller and larger crack sizes, respectively. In both cases the highest error in the solution came at the corners, but the error was extremely small compared to that of the models with external cracks. Neither case converged as nicely as the simulation of the block geometry without cracks. As observed in all block simulations the horizontal displacement data along the vertical patch boundary was extremely inaccurate.

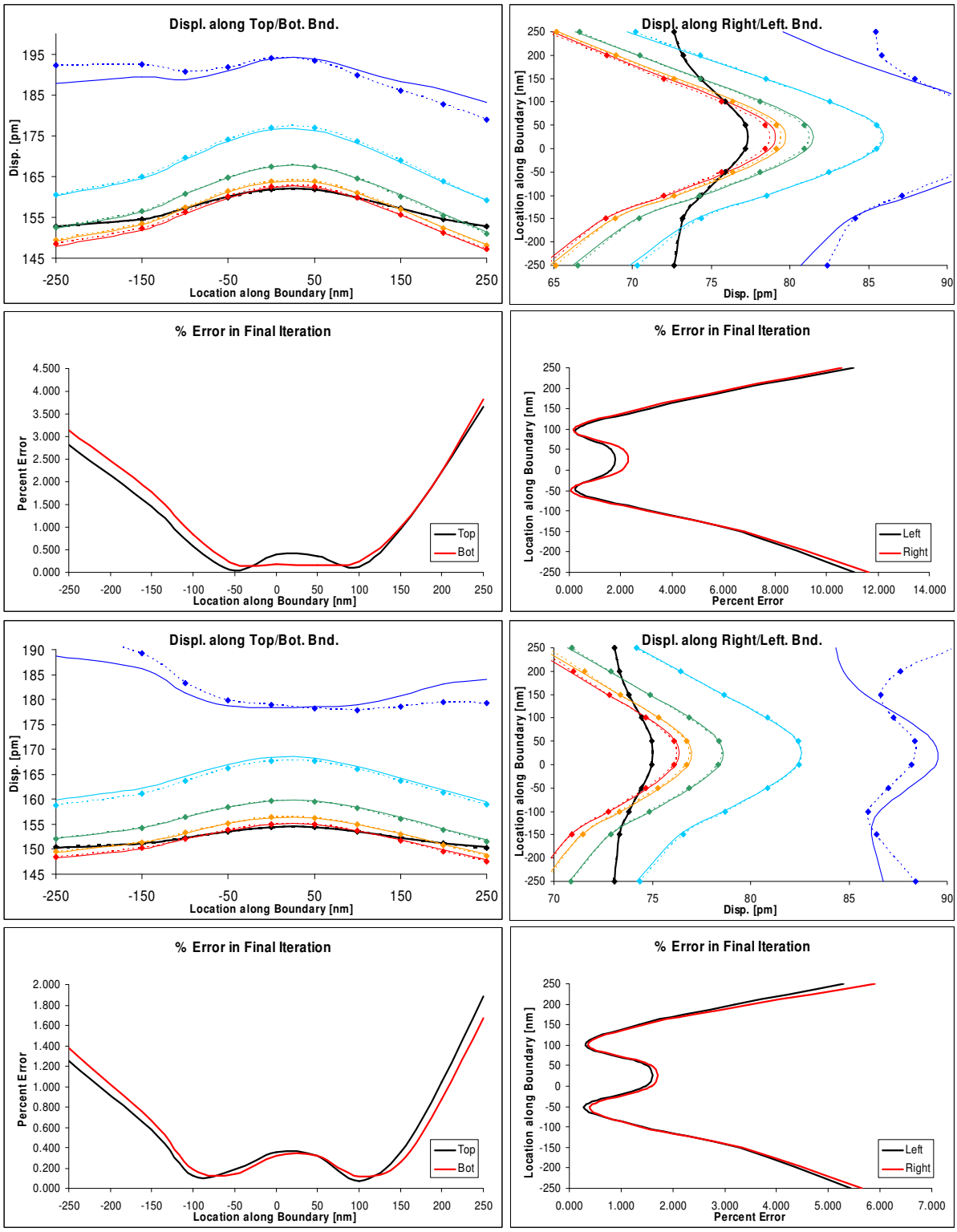

Figure 7.8: Convergence and Percent Error of FEA-FEA of block geometry with internal crack 25x100nm (top) and 10x70nm (bottom) under loading case (a).

CHAPTER 8

CONCLUSIONS AND FUTURE WORK

8.1 Conclusions

The accuracy and convergence of each scenario modeled can be founding Table 8.1. The focus of the research present in this paper was to determine the feasibility and robustness of a coupled ENM-FEA scheme. The coupled analysis was tested against 32 different scenarios and the results of each simulation were presented in this report. This chapter will highlight the trends that appeared in the majority of the simulations as well

Table 8.1: A summary of the accuracy and convergence of each model.

	Geo./Mat.Prop.	Scheme	Loading Case	Percent Accuracy	Percent Convergence
Basic Geometry - No Cracks	Block - Iso	FEA-FEA	a	0.56	0.90
			b	1.72	0.85
			c	1.10	0.90
		FEA-ENM	a	1.90	1.29
			b	1.62	0.76
			c	1.50	2.00
	Block - Ani	FEA-FEA	a	0.50	0.80
			b	1.85	0.80
			c	0.55	0.75
		FEA-ENM	a	0.80	0.74
			b	2.00	0.88
			c	1.90	1.50
	Stick - Iso	FEA-FEA	a	0.37	0.36
			b	0.35	0.37
			c	1.80	0.37
		FEA-ENM	a	0.31	0.41
			b	0.39	0.47
			c	6.00	n/a
	Stick - Ani	FEA-FEA	a	0.26	0.26
			b	0.48	n/a
		FEA-ENM	a	0.23	0.27
			b	0.52	n/a
Geometry with Cracks	Internal - Iso	FEA-FEA	Stick (25x100nm)	0.42	0.05
			Block (25x100nm)	1.30	0.90
			Block (10x70nm)	0.62	0.80
		FEA-ENM	Stick (25x100nm)	1.42	n/a
	External - Iso	FEA-FEA	Block (1 crack)	9.00	0.63
			Block (2 cracks)	7.40	0.20
		FEA-ENM	Block (1 crack)	9.25	0.26
			Block (2 cracks)	9.00	0.23

as point out the major shortcomings in the analysis scheme.

8.1.1 Positive Overlying Trends in Simulation Results

The simulation results prove the force and displacement values at the patch boundaries can converge accurately to the solution value, which is particularly obvious in the simplest geometries and loading cases. The coupled analysis of the two and four-sided transverse models with an internal crack demonstrated the ability of the schemes to evaluate parts with cracks.

8.1.2 Negative Overlying Trends in the Simulation Results

The most prevalent deficiency in the simulation results was the inability to accurately capture the force outputs trends near the interfacial boundary extremities. This shortcoming was not completely unexpected. The interface boundaries meet at right angles creating sharp corners. The singularity caused at the corner vertex is the same as would be at the tip of a crack. FEA's inability to model the stress fields in the immediate vicinity of a crack is well documented and this limitation is reflexively related to the analysis of sharp corners. It was hoped that the coupled analysis scheme would sufficiently mitigate the stress concentrations caused by the corners through successive iterations. The coupled analysis scheme did reduce the stress concentration effect of the corners, as demonstrated by the convergence diagrams, but not enough to account for subtle changes in forces near the corners that resulted from complex loadings that could be present in future simulations.

Rounding the interface corners with a 50nm radius curve failed to reduce the effects corner effects. This was partially due to the imprecision of the interpolation file

used to apply the displacement values to the curved surface. A much smaller curve not participating in the data exchange may have been more effectively at reducing the effect of the corners and could be tried in future simulations.

The force and displacement convergence and accuracy along the vertical interface boundaries was also poor throughout all the different scenarios. This could be attributed to a number of different conditions and is most likely a combination of all of them. There were no external loads applied to the vertical boundaries in the outer region. Consequently all the horizontal force and displacement values were a result of the contraction caused by the externally applied vertical force. The convergence of the top and bottom boundaries in the vertical direction, parallel to the applied force, was generally good. It seems reasonable to suspect that a force applied perpendicular to the vertical boundaries would increase its convergence and accuracy. The extremities of the vertical boundaries are also susceptible to the corner effects mentioned in the previous paragraph.

In many of the symmetrical model under loading cases (a) and (b) the force and displacements results are not symmetrical, most noticeable in early iterations. This observation does tend to diminish with continued iteration, but the effects are still present in the final iteration as shown by the asymmetric Percent Error graphs. These asymmetries could be caused by poor or inadequate rigid body constraints or from the force anomalies that occur at the corners.

8.1.3 Observations During Testing

The coupled analysis schemes were often interrupted by execution errors. The errors always occurred during the FEA analysis of a component. The component could

often be successfully reanalyzed with FEA immediately after the error without making any changes to the input. It should be noted that the coupled analysis schemes did not converge as accurately when continued after the error message (even when no changes were made to the input data). Comparing the results of an interrupted and uninterrupted simulation of the anisotropic stick model shows this phenomenon. The simulation results are presented in Appendix A6-A7. The uninterrupted model converged significantly more accurately.

The effect of the constraints and loading were determined to be important. The ENM is very difficult to constrain in its current condition. Furthermore, excessive caution must be used when constraining asymmetric geometries and/or models with asymmetric loads in order to prevent rigid body motion without imposing perturbations to the stress field that would adversely influence the analysis of the model. This observation came about when massive rigid body motion was observed during an ENM-FEA of the four-sided transverse model with an internal crack in the ENM.

8.2 Future Work

The advised future work is directed at addressing the deficiencies in the current modeling techniques, and aimed at increasing the versatility of the coupled analysis scheme.

8.2.1 FEA

The stress concentrations resulting at the patch boundaries need to be mitigated. This could be accomplished through increased data conditioning or changing the model geometry to eliminate sharp corners. Inputting and outputting displacement data from a

curved boundary could prove difficult and the current technique of implementing interpolation files to input displacement values along boundaries in FEA proved inadequate (on curved surfaces) in preliminary testing.

8.2.2 ENM

The ability to easily apply arbitrary constraints to the ENM is necessary and would facilitate the modeling of different geometries and loading conditions. Further research into the how the values of the vertical, horizontal, and diagonal spring constants effect the overall stiffness of the ENM are warranted and necessary for controlling the models' behavior. Particular attention needs to be allocated to controlling the displacement of the boundary nodes in the ENM in order to prevent inaccurate displacement outputs, or stress concentration within the patch, resulting from the difference in stiffness between them and other nodes in the system.

8.2.3 Analysis Scheme Related

Further exploration on the inaccurate convergence along the vertical interface boundaries is necessary. The effects of subjecting the model to biaxial external loading could be pertinent to investigating this issue.

A switch to eliminate the cutoff and relaxation algorithm as the convergence of the solution approaches equilibrium would be novel. As would an algorithm that could stop the iterations once the outputs had sufficiently converged (rather than just set the number of iterations manually).

APPENDIX A

THE CUTOFF ALGORITHM: MATLAB CODE

```
function [out] = cutoff(in, sol, beta)
% 'in' is the matrix that needs conditioning
% 'sol' is the solution input matrix
% 'beta' is the cutoff percentage
% 'out' is the output matrix

% this determines the size of the input matrix
sz1 = size(in, 1);
sz2 = size(in, 2);

if sz2>sz1
   sz = sz2;
else
   sz = sz1;
end

% this section applies the cutoff algorithm
for i=1:sz
   if sign(sol(i))>0
      pmax=(1+beta)*sol(i);
      pmin=(1-beta)*sol(i);
      if in(i)> pmax
         out(i) = pmax;
      elseif in(i)<pmin
         out(i) = pmin;
      else
         out(i) = in(i);
      end
   elseif sign(sol(i))<0
      nmax = (1-beta)*sol(i);
      nmin = (1+beta)*sol(i);
      if in(i)>nmax
         out(i) = nmax;
      elseif in(i)<nmin
         out(i) = nmin;
      else
         out(i) = in(i);
      end
   else
      out(i) = 0;
   end
end
```

APPENDIX A

THE CUTOFF ALGORITHM: VALIDATION

The original matrix entered was random (represented by the dotted line). It's average was determined and entered as the 'solution' in the cutoff algorithm. The cutoff algorithm compares the discrete values of the input matrix to the corresponding discrete values of the solution matrix. If the values fell outside the region determined by the cutoff factor (0<=beta<=1) the maximum value (beta*sol(i)) is applied in place of the original value. Results are shown for the following 4 cases listed below:

1. A positive 1xn matrix
2. A negative 1xn matrix
3. A positive nx1 matrix
4. A negative nx1 matrix

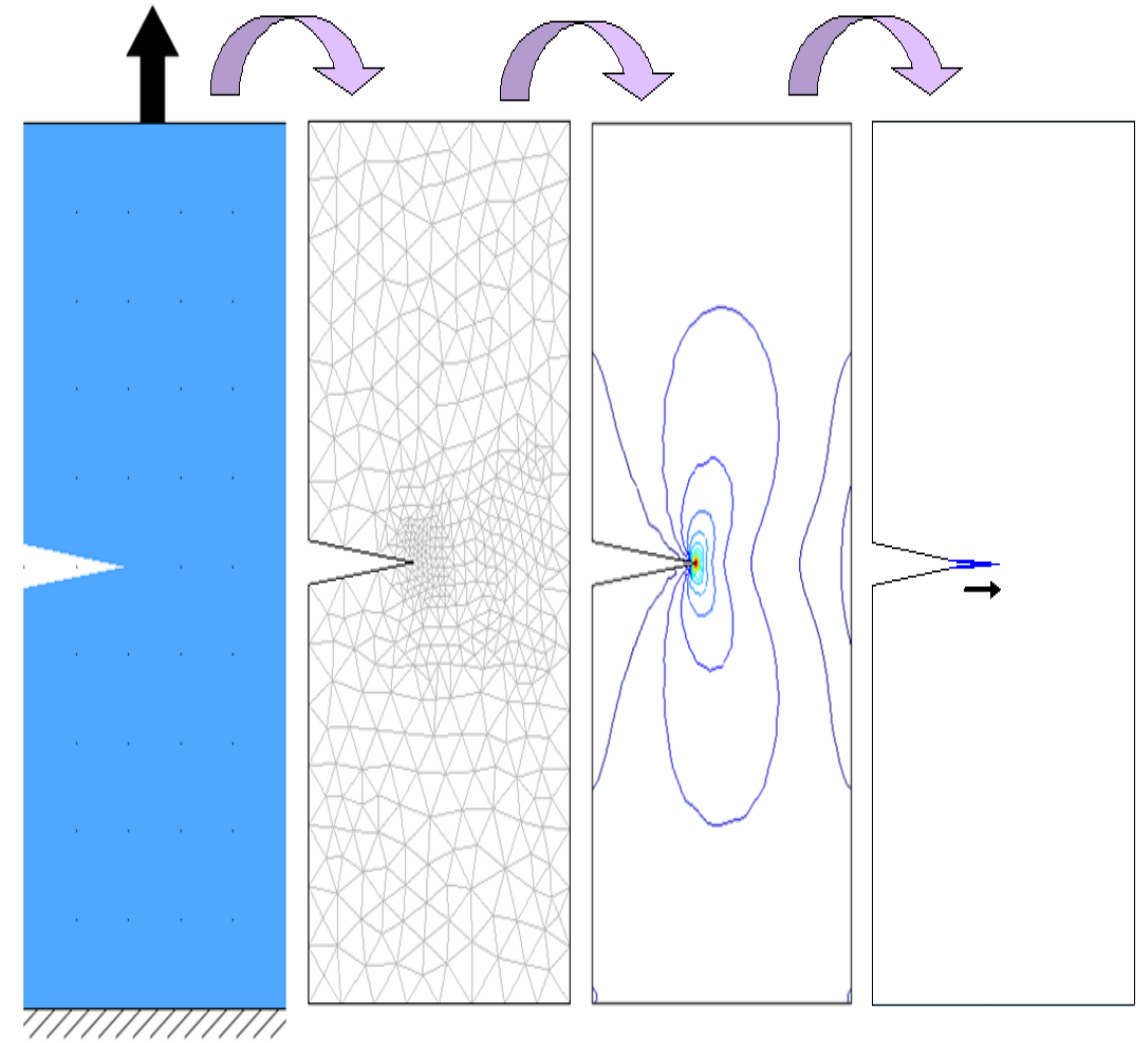

Figure A.1: Validation of the cutoff algorithm.

APPENDIX B

RELAXATION ALGORITHM: MATLAB CODE

```
function [out] = relaxation(old, new, alpha)
% 'old' is the output from the previous iteration
% 'new' is the output from the most recent iteration
% 'alpha' is the percent change allowed
% 'out' is the matrix that will be used in the next iteration

% this determines the size of the input matrix
stop1 = size(old,1);
stop2 = size(old,2);
if stop1>=stop2
   stop = stop1;
else
   stop = stop2;
end

% this section applies the relaxation algorithm
for i=1:stop
   if sign(old(i))>sign(new(i)) || sign(old(i))<sign(new(i))
      % if the values have different signs
      out(i) = old(i) - alpha*(old(i)-new(i));
   else
      % if the values have the same sign
      out(i) = old(i) + alpha*(new(i)-old(i));
   end
end
```

The relaxation algorithm was validated against the following 8 scenarios:

1. A positive 1xn matrix taking positive step (2 times itself)
2. A negative 1xn matrix taking negative step (2 times itself)
3. A positive nx1 matrix taking positive step (2 times itself)
4. A negative nx1 matrix taking negative step (2 times itself)
5. A positive 1xn matrix taking negative step (-2 times itself)
6. A negative 1xn matrix taking positive step (-2 times itself)
7. A positive nx1 matrix taking negative step (-2 times itself)
8. A negative nx1 matrix taking positive step (-2 times itself)

*'steps' indicate iteration step 1 and step 2 are the 'old' and 'new' matrix in the code
The results are shown below and on the next page:

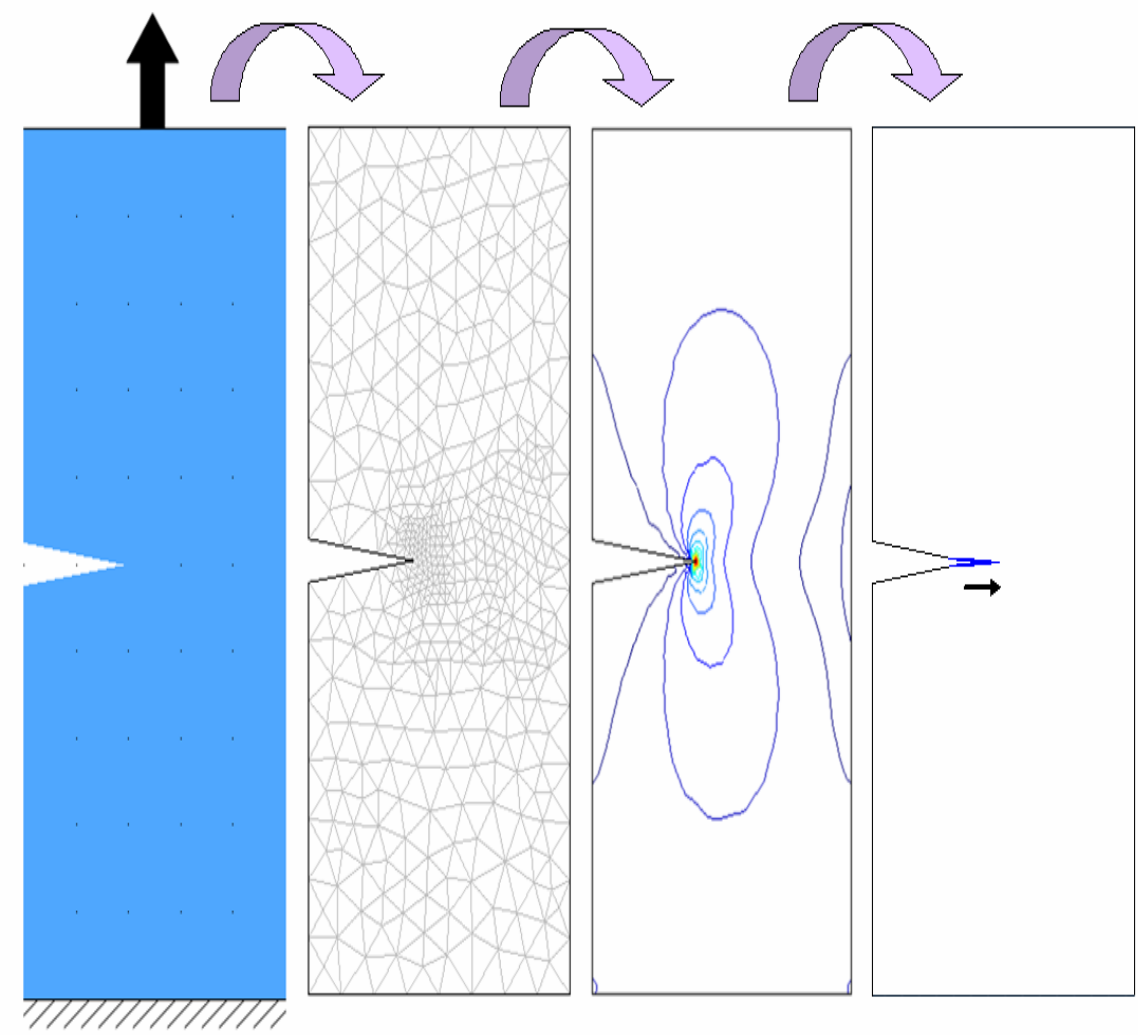

Figure B.2: Validation of the relaxation algorithm; case 1-4.

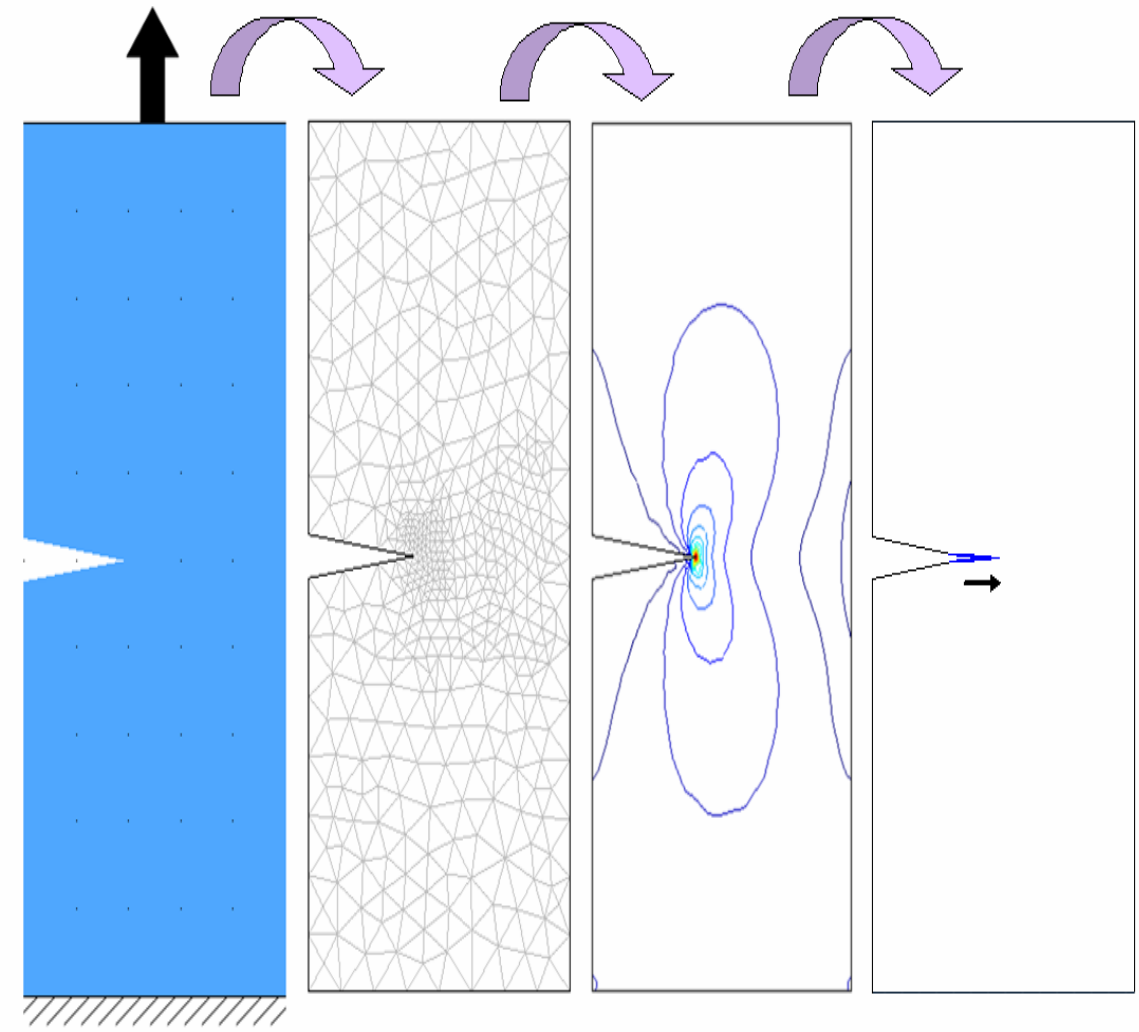

Figure B.2: Validation of the relaxation algorithm; case 5-8.

APPENDIX C

EFFECTS OF INTERRUPTED ITERATIONS

The results presented below are from the ENM-FEA of the anisotropic two-sided transverse interface model under a uniform external loading condition. The first set of plots is from the interrupted simulation and the second set is from the uninterrupted simulation. The interrupted simulation was continued from the point of interruption (FEA of the outer region) without any modification to the input/output data.

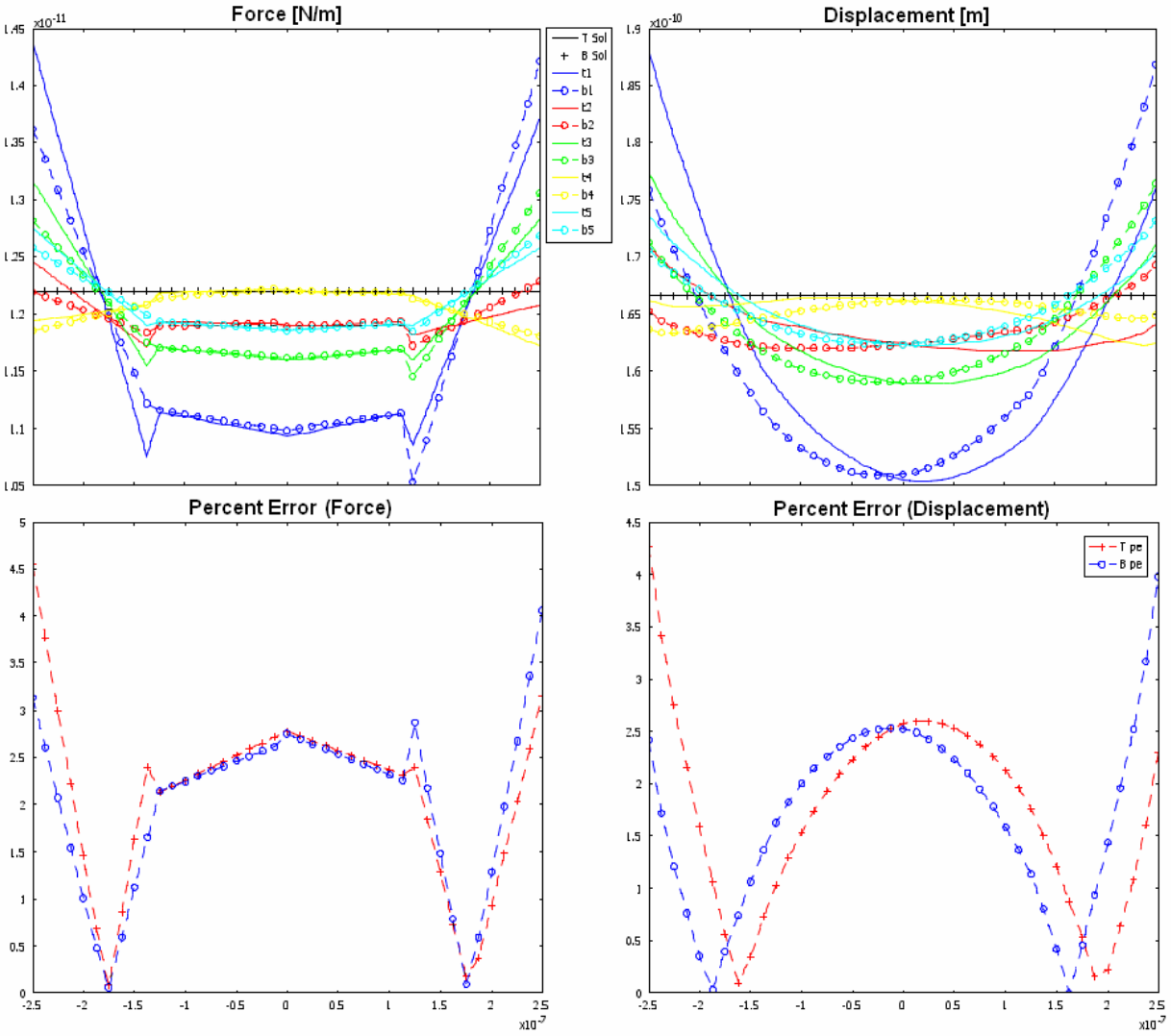

Figure C.3: Results from an interrupted simulation. Note the poor final convergence.

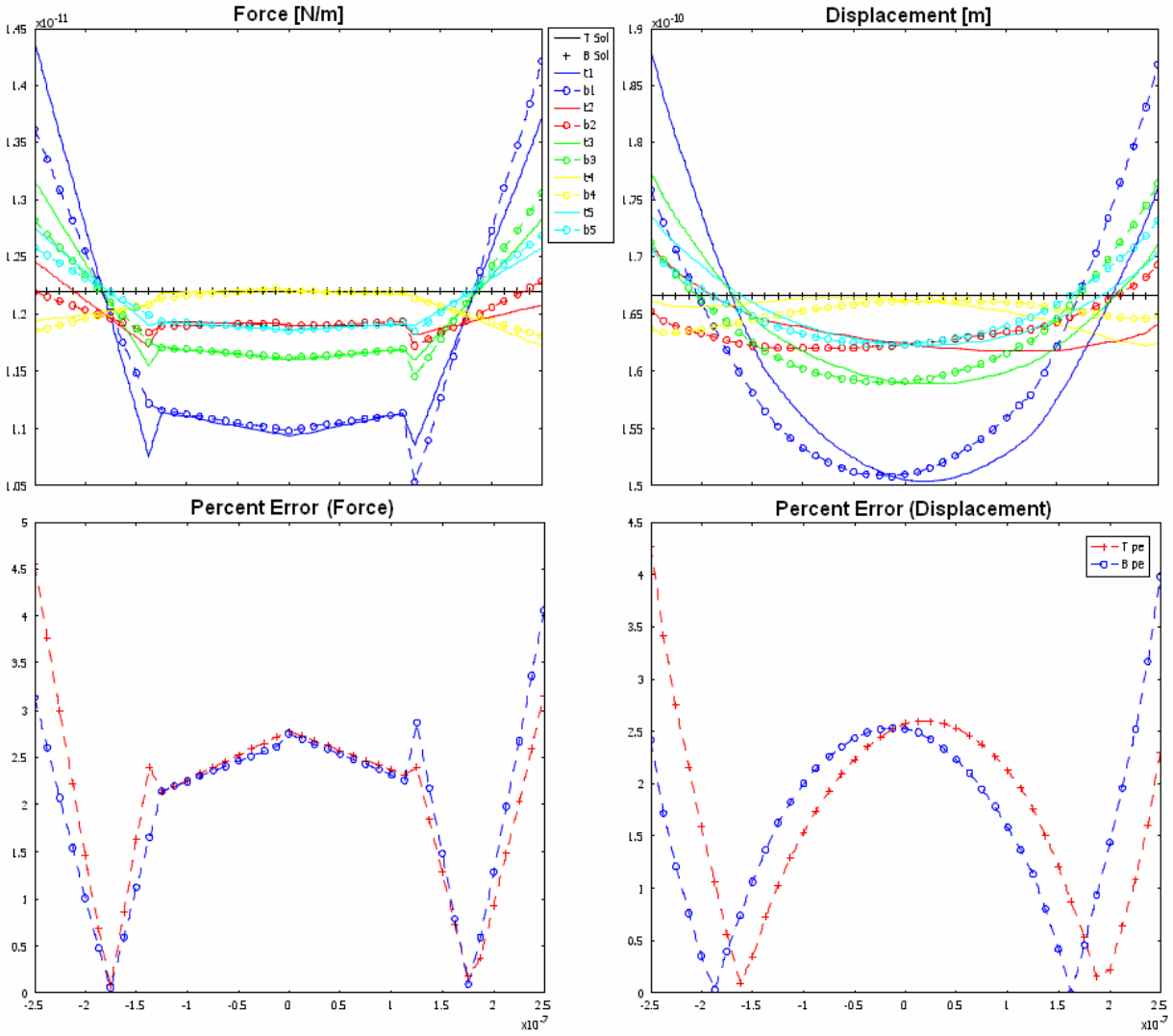

Figure C.2: Results from an uninterrupted simulation. Note the better convergence than the interrupted case.

REFERENCES

1 A. Balazs, T. Emrick and T. Russell, "Nanoparticle Polymer Composites: Where Two Small Worlds Collide", *Science*, vol. 314, 2006, pp. 1107-1110.

2 R. Truss, "Fracture Mechanics of Polymers", University of Queensland.

3 D. Broek, *The Practical Use of Fracture Mechanics*, Kluwer Academic Publishers, Galena, OH, 1988.

4 M. Ashby, *Materials Selection in Mechanical Design*, Butterworth Heinemann, Burlington, MA, 1999. pp. 43-47.

5 T. Anderson, *Fracture Mechanics: Fundamentals and Applications*, CRC, Boston, 1995.

6 A. Rosenfield, "Fracture Mechanics", *Wikipedia*, 2006.

7 H. Bui and C. Stolz, "Damage Theories for Brittle and Ductile Materials" *Fracture of Non-Metallic Materials*. K. Herrmann and L. Larsson: D. Reidel Publishing Company, Boston, MA. pp. 33-46

8 J. Lemsitre and R. Desmorat, *Engineering Damage Mechanics*, Springer, 2005.

9 J. Williams, "Fracture Mechanics of Polymers and Adhesives" *Fracture of Non-Metallic Materials*. K. Herrmann and L. Larsson: D. Reidel Publishing Company, Boston, MA. pp. 227-255

10 K. Bowman, *Mechanical Behavior of Materials*, Wiley, 2003.

11 http://www.ndt-ed.org *Fracture Toughness*. Iowa State University. 2001.

12 T. Courtney, *Mechanical Behavior of Materials*, Waveland Press, Long Grove, IL, 2000.

13 A. Saxena, *Nonlinear Fracture Mechancics*, CRC, 1998. pp. 81-106.

14 S. Suresh, *Fatigue of materials*, Cambridge University Press, Cambridge, 1991.

15 http://www.efunda.com *The J Integral*. Engineering Fundamentals. 2007.

16 W. Liu, J. Shen, Z. Wang, F. Lu and M. Xu, "The deformation mechanism of polyphenylquinoxaline films", *Polymer*, vol. 42, 2001, pp. 7461-7464.

17 R. Hyers, S. Nair, M. Kim and J. Rothstein, "NSF Grant Proposal", UMass: Amherst, MA. 2005

18 S. Wong, S. Nair and L. Goettler, "Fracture resistance of polyblends and polyblend matrix composites: Part I: Unreinforced and fibre-reinforced nylon 6,6/ABS polyblends", *Journal of Materials Science*, vol. 32, 1997, pp. 5335-5346.

19 L. Chen, S. Wong and S. Pisharath, "Fracture Properties of Nanoclay-Filled Polypropylene", *Journal of Applied Polymer Science*, vol. 88, 2003, pp. 3298-3305.

20 S. Subramaniam, S. Nair and L. Goettler, "Fracture resistance of polyblends and polyblend matrix composites: Part II: Role of rubber phase in nylon 6,6/ABS alloys", *Journal of Materials Science*, vol. 32, 1997, pp. 5347-5354.

21 A. Lesser, "Polymer Toughening Mechanisms", Class Notes: Polymer Fracture and Heterogeneous Media: Amherst, MA. 2006

22 S. Balakrishnan and D. Raghavan, "Acrylic, Elastomeric, Particle-Dispersed Epoxy-Clay Hybrid Nanocomposites: Mechanical Properties", *Macromolecular Rapid Communications*, vol. 25, 2004, pp. 481-485.

23 T. Kawaguchi and R. Pearson, "The effect of particle-matrix adhesion on the mechanical behavior of glass filled epoxies. Part 2. A study on fracture toughness", *Polymer*, vol. 44, 2003, pp. 4239-4247.

24 A. Lazzeri and C. Bucknall, "Dilational bands in rubber toughened polymers", *Journal of Materials Science*, vol. 28, 1993, pp. 6799-6808.

25 A. Lazzeri and C. Bucknall, "Applications of dilatational yielding model to rubber toughened polymers", *Polymer*, vol. 36, 1995, pp. 2895.

26 A. Zerda and A. Lesser, "Intercalated Clay Nanocomposites: Morphology, Mechanics, and Fracture Behavior", *Journal of Polymer Science: Part B: Polymer Physics*, vol. 39, 2001, pp. 1137-1146.

27 S. Subramaniam, S. Nair and L. Goettler, "Fracture resistance of polyblends and polyblend matrix composites: Part III: Role of rubber type and location in nylon 6,6/SAN composites", *Journal of Materials Science*, vol. 33, 1998, pp. 3455-3464.

28 http://biomechanics.ecs.umass.edu/composites.html# *Molecular Mechanisms of Failure in Multiscale polymer Composites*. M. Kim.

29 A. Gonzales-Herrera and J. Zapatero, "Influence of minimum element size to determine crack closure stress by the finite element method", *Engineering Fracture Mechanics*, no. 72, 2005, pp. 337-355.

30 M. Ortiz, "Computational micromechanics", *Computational Mechanics*, no. 18, 1996, pp. 321-338.

31 W. Callister, *Fundamentals of Materials Science and Engineering: An Integrated Approach*, John Wiley & Sons, Inc,, Hoboken, 2005.

32 J. Zhou and K. Komvopoulos, "Nanoconfinement Effect on the Mechanical Behavior of Polymer Thin Films", Materials Research Society 2005 Spring Meeting Proceddings: 2005

33 K. Schroter, "Comment on 'Novel approach to the analysis of the non-Debye dielectric spectrum broadening'", *Physica A*, vol. 326, 2003, pp. 605-606.

34 G. Odegard, T. Gates, K. Wise, C. Park and E. Siochi, "Constitutive modeling of nanotube-reinforced polymer composites", *Composites Science and Technology*, vol. 63, 2003, pp. 1671-1687.

35 CFG, *FRANC3D Concepts & Users Guide - Version 2.6*, Ithaca, NY, 2003.

36 http://www.cfg.cornell.edu/ *Cornell Fracture Group*. 2006.

37 P. Krysl and T. Belytschko, "The element free galerkin method for dynamic propagation of arbitrary 3-D cracks", *International Journal for Numerical Methods in Engineering*, no. 44, 1999, pp. 767-800.

38 T. Ingraffea and W. Wawrzynek, "Introduction to FRANC2D, FRANC2D/L and FRANC3D", ASTM Workshop on Computational Fracture Mechanics for Composites: Salt Lake City. 2004

39 T. Liu, G. Liu and Q. Wang, "An Element-Free Galerkin-Finite Element Coupling Method for Elasto-Plastic Contact Problems", *Journal of Tribology*, vol. 128, 2006, pp. 1-9.

40 E. Weisstein, "Finite Element Method", From *MathWorld - - A Wolfram Web Resource. http://mathworld.wolfram.com/FiniteElementMethod.html*, 2007.

42 B. Carter, "Parallel FEM Simulation of Crack Propagation - Challenges, Status, and Perspectives".

43 B. Carter, P. Wawrzynek and A. Ingraffea, "Automated 3D Crack Growth Simulation", Cornell: 2003

44 J. Lee, G. Buxton and A. Balazs, "Using nanoparticles to create self-healing composites", *Journal of Chemical Physics*, vol. 121, no. 11, 2004, pp. 5531-5540.

45 M. Kim, W. Li, B. Shapiro and G. Chirikjian, "A Comparison Between Elastic Network Interpolation and MD Simulations of 16S Ribosomal RNA", *Journal of Biomolecular Structure & Dynamics*, vol. 21, no. 3, 2003, pp. 1-11.

46 Y. Jang, J. Jeong and M. Kim, "UMMS: constrained harmonic and anharmonic analyses of macromolecules based on elastic network models", *Nucleic Acids Research*, vol. 34, 2006, pp. W57-W62.

47 M. Kim, "Elastic Network Models of Biomolecular Structure and Dynamics", *Thesis Dissertaion - John Hopkins University*, 2004.

48 J. Jeong, Y. Jang and M. Kim, "A connection rule for alpha-carbon coarse-grained elastic network models using chemical bond information", *Journal of Molecular Graphics and Modeling*, vol. 24, 2006, pp. 296-306.

49 M. Kim, Y. Jang and J. Jeong, "Using Harmonic Analysis and Optimization to Study Macromolecular Dynamics", *International Journal of Control, Automation, and Systems*, vol. 4, no. 3, 2006, pp. 382-393.

50 G. Odegard, T. Clancy and T. Gates, "Modeling of the mechanical properties of nanoparticle/polymer composites", *Polymer*, no. 46, 2004, pp. 553-562.

51 G. Buxton, C. Care and D. Cleaver, "A lattice spring model of heterogeneous materials with plasticity", *Modeling and Simulation in Materials Science and Engineering*, no. 9, 2001, pp. 485-497.

52 COMSOL, *COMSOL Multiphysics User's Guide*, 2005.

53 A. Atilgan, S. Durell, R. Gernigan, M. Demire, O. Keskin and I. Bahar, "Anisotropy of fluctuation dynamics of proteins with an elastic network model", *Biophysical Journal*, vol. 80, no. 1, 1996, pp. 505-515.

54 *Annual Book of ASTM Standards*, ASTM, West Conshohocken, 1999.